https://doi.org/10.5194/egusphere-2026-3314
Preprint. Discussion started: 16 June 2026

Observation-based analysis of horizontally oriented ice crystals using dual-angle polarization lidar and cloud Doppler radar in Beijing

Zhaolong Wu[1, 2], Patric Seifert[2], Yun He[2, 3, 4], Holger Baars[2], Cristofer Jimenez[2, 5], Chengcai Li[1, †], Jing Li[1], Albert Ansmann[2], and Chuanfeng Zhao[1]

[1]Department of Atmospheric and Oceanic Sciences, School of Physics, Peking University, Beijing 100871, China
[2]Leibniz Institute for Tropospheric Research, Leipzig 04318, Germany
[3]School of Earth and Space Science and Technology, Wuhan University, Wuhan 430072, China
[4]State Observatory for Atmospheric Remote Sensing, Wuhan 430072, China
[5]Universidad de Concepción, Concepción 4070386, Chile
[†]deceased, 21 April 2025

Correspondence to: Chuanfeng Zhao (cfzhao@pku.edu.cn)

Abstract. Ice crystal orientation strongly influences cloud radiative properties and remote sensing retrievals, but long-term, high-resolution quantitative observations remain scarce. This study presents comprehensive case studies and statistical analyses of horizontally oriented ice crystals (HOICs) based on full-year (2022) synergistic observations in Beijing, China, combining a zenith-pointing micropulse lidar, a collocated 15° off-zenith polarization lidar, and a Ka-band cloud Doppler radar. Applying a novel height-resolved classification method based on dual-angle polarization lidars, HOICs are identified with high spatiotemporal resolution. HOICs are found to be common, accounting for 15.0 % of all ice-containing cloud data points annually and peaking at 24.6 % in summer, with maximum occurrence at temperatures from −20 °C to −10 °C. Macroscopically, typical HOIC layers exhibit horizontal extents of 10–100 km and durations of several hours within their optimal formation temperature ranges. Furthermore, the Euclidean-distance analysis between HOICs and past overlying cloud layers revealed a strong linkage of HOIC occurrence to supercooled liquid water clouds (SWCs), being much closer to HOIC events than randomly oriented ice crystals (ROICs). Dynamically, cloud radar observations further reveal that HOICs preferentially occur in stable environments with turbulent eddy dissipation rates below 10^{-2} m² s^{-3} and exhibit lower fall velocities than ROICs. Estimates based on radar-observed vertical velocity indicate typical HOIC equivalent diameters of approximately 1200 μm with Reynolds numbers predominantly below 100. The findings provide key observational constraints for improving ice cloud microphysics and orientation parameterizations in numerical models.

1 Introduction

Most climate models and radiative transfer calculations commonly assume the presence of randomly oriented ice crystals (ROICs) (Yang et al., 2005; Klotzsche and Macke, 2006). In the real atmosphere, however, ice crystals do not always fall in random orientations. Under relatively stable thermodynamic and dynamical conditions, planar or elongated ice crystals, including hexagonal plates, columns and dendrites, may undergo aerodynamic rotational stabilization, aligning their largest cross sections approximately perpendicular to the fall direction and thereby forming so-called horizontally oriented ice crystals

https://doi.org/10.5194/egusphere-2026-3314
Preprint. Discussion started: 16 June 2026

(HOICs) (Bréon and Dubrulle, 2004; Noel and Chepfer, 2010; Pruppacher and Klett, 2010; Westbrook et al., 2010). The existence of such oriented particles is also consistent with a variety of atmospheric optical phenomena, including sun dogs, circumzenithal arcs, circumhorizon arcs, light pillars, and tangent arcs, which require specific populations of HOICs in the atmosphere (Tape, 1994; Saito and Yang, 2019).

HOICs are important because they affect both cloud radiative properties and the interpretation of remote-sensing observations. Owing to their angle-dependent specular reflection, HOICs can substantially modify the ice cloud scattering phase functions (Zhou et al., 2012b; Saito and Yang, 2019) and enhance the reflection of shortwave radiation relative to randomly oriented particles (Takano and Liou, 1989). Their preferred horizontal posture also increases aerodynamic drag and reduces terminal fall velocity, which may influence sedimentation and the microphysical evolution of ice clouds (Mitchell, 1996; Westbrook, 2008; Heymsfield et al., 2017; Zeng et al., 2022). From the remote sensing perspective, HOICs can introduce substantial biases into cloud property retrievals when particle orientation is ignored. For example, neglecting horizontally aligned ice crystals may lead to overestimates of ice water path and cirrus optical depth in some retrieval frameworks (Gong and Wu, 2017; Kaur et al., 2022; Masuda and Ishimoto, 2004). In addition, sun glints associated with HOICs can affect cloud detection and cloud optical thickness retrievals from passive satellite observations (Várnai et al., 2024).

HOICs are also a challenge for cloud-phase determination based on lidar depolarization. In zenith-pointing polarization lidar observations, specular reflection from HOICs produces strongly enhanced backscatter together with near-zero depolarization ratios (Sassen, 1991; Seifert, 2011; He et al., 2021). These optical signatures closely resemble those of dense supercooled liquid water clouds (SWCs), which also exhibit high backscatter and very low depolarization ratios (Platt, 1978; Seifert, 2011). Consequently, HOICs are prone to being misclassified as liquid cloud layers in phase identification that rely solely on zenith-pointing polarization lidar observations (Wang et al., 2022). This structural ambiguity poses a challenge for extensive operational zenith-pointing lidar networks, including AD-Net (Asian Dust and Aerosol Lidar Observation Network), MPLNET (Micro-Pulse Lidar Network), and CARLNET (China Aerosol Raman Lidar Network) (Shimizu et al., 2016; Welton et al., 2001; Shao et al., 2025). These limitations hinder the accurate interpretation of mixed-phase cloud structure and motivate the need for observation strategies that better separate HOIC from SWC signatures.

A range of observational approaches has been used to investigate HOICs, but important limitations remain. Fundamental questions persist; for instance, the reported occurrence of HOIC varies significantly among different studies (Westbrook et al., 2010). Aircraft observations provide in-situ information but are constrained by limited sampling volumes and by disturbances to the ambient flow field during sampling (MacPherson and Baumgardner, 1988). Laboratory studies can characterize the fall behavior of ice crystal analogues under controlled conditions, but they cannot fully reproduce the complexity of natural clouds (Auguste et al., 2013; Stout et al., 2024). Passive satellite observations have detected HOIC-related signals through sun glints or polarization-based quantities (Chepfer et al., 1999; Noel and Chepfer, 2004; Marshak et al., 2017; Varnai et al., 2020; Gong and Wu, 2017; Zeng et al., 2019), while CALIOP (Cloud-Aerosol Lidar with Orthogonal Polarization) has provided valuable large-scale information on their global distribution (Hu et al., 2009; Noel and Chepfer, 2010; Zhou et al., 2012a). However, satellite observations generally lack the fine vertical resolution and continuous temporal sampling required to examine the full

https://doi.org/10.5194/egusphere-2026-3314
Preprint. Discussion started: 16 June 2026

evolution of HOICs within specific cloud layers (Ross et al., 2017). In particular, earlier spaceborne dual-angle approaches were based on non-simultaneous viewing configurations or layer-integrated quantities (Kikuchi et al., 2021; Zhou et al., 2012a), which limited their suitability for robust statistical analysis of HOIC occurrence and vertical structure. Ground-based lidars can provide high spatiotemporal resolutions for HOICs, yet previous off-zenith or scanning lidar studies face some limitations. Most of these previous studies did not provide range-resolved HOIC products and were limited to manual case-based analyses (He et al., 2021) or could not perform simultaneous zenith and off-zenith measurements (Platt, 1978; Sassen, 1991; Kokhanenko et al., 2020). Although Westbrook et al. (2010) systematically investigated specular reflection of cloud layers using a simultaneous vertical ceilometer and off-zenith lidar with collocated radars, their lidars operated at different wavelengths and lacked depolarization capabilities. Consequently, long-term, high spatiotemporal range-resolved statistical constraints on HOIC occurrence and environmental controls remain scarce, and synergistic observations of HOICs combining polarization lidar and cloud radar are also very limited.

In our previous study, we introduced a range-bin-resolved method for identifying HOICs from the angle dependence of specular reflection using a ground-based dual-angle polarization lidar configuration consisting of a zenith-pointing micropulse lidar (MPL) and a collocated 15° off-zenith-pointing lidar at the same wavelength (Wu et al., 2025). The study mainly focused on methodological development and representative cases, whereas the long-term statistical behavior of HOICs in the real atmosphere remains insufficiently quantified. In particular, key questions remain regarding their annual and seasonal occurrence, diurnal variability, and macrophysical characteristics, whereas their preferred thermodynamic and dynamical behaviours and their spatial relationships with overlying supercooled liquid water layers, which provide the necessary thermodynamic environment for oriented plate-like crystals (Westbrook et al., 2010), have not yet been systematically quantified at long timescales.

To address these questions, this study presents a year-long statistical characterization of HOICs, together with selected case analyses, using continuous dual-angle polarization lidar and cloud Doppler radar observations collected in Beijing, China, in 2022. By combining these measurements with ERA5 reanalysis and radiosonde data, we investigate (1) the occurrence and variability of HOICs, including their seasonal, diurnal, and macrophysical characteristics, (2) their relationships with environmental conditions and overlying SWCs, and (3) their radar-derived dynamical and microphysical signatures. The paper is arranged as follows. Section 2 introduces the observational data and methodology. Section 3 first presents an exemplary case and then representative case studies under different cloud-top temperatures. Section 4 provides the year-long statistical results. Section 5 summarizes the main conclusions.

2 Data and Methodology

2.1 Observations and ancillary data

In this study, the main observation instruments are a zenith-pointing micropulse lidar (MPL) and a collocated 15° off-zenith-pointing AVORS lidar (manufactured by AVORS Technology Company). Both lidars operate at 532 nm wavelength, have

https://doi.org/10.5194/egusphere-2026-3314
Preprint. Discussion started: 16 June 2026

depolarization capabilities and a range resolution of 15 m. The raw temporal resolutions are 15 s for the MPL and either 10 s or 60 s for the AVORS lidar. Additionally, a 33.44 GHz Ka-band zenith-pointing cloud Doppler radar at the same site is used to further investigate the HOIC events, with its quality control following Ding et al. (2022). The vertical and temporal resolutions of the cloud radar are 30 m and 13 s, respectively. Environmental variables, including relative humidity, temperature, and horizontal wind speed and direction, are provided by ERA5 reanalysis data extracted at the Peking University Physics Building grid (116.3° E, 40.0° N) and radiosonde profiles from the Beijing Nanjiao Observatory (116.37° E, 39.80° N; WMO no. 54511). Further details are provided in Sect. 2 of our previous publication (Wu et al., 2025). The total observation period covers 354 days in 2022.

2.2 Relaxed cloud mask

The specialized classification algorithm detailed in our previous study (Fig. 2 in Wu et al., 2025) is applied to classify cloud phase for the identified cloud range bins. In our previous study, the cloud bins identified by both the zenith-pointing and off-zenith-pointing lidars are used. Here we refer to it as the "rigorous" cloud mask.

In general, the off-zenith-pointing lidar shows a lower signal-to-noise ratio (SNR) than the zenith-pointing MPL at the same altitude bin. First, the off-zenith-pointing lidar was deployed outdoors without a container and was therefore more susceptible to solar background noise, whereas the MPL was housed inside a container with a lens hood to reduce such contamination. Second, for a given altitude, the off-zenith geometry leads to a longer atmospheric path length and hence stronger attenuation. Moreover, HOICs produce much stronger backscatter in the zenith-pointing lidar than in the off-zenith-pointing lidar, making cloud-layer detection more easily triggered in the zenith observations (Zhao et al., 2014; Wu et al., 2025). Consequently, the zenith-pointing lidar often detects more HOIC range bins in many cases.

In this way, we find that using a rigorous cloud mask underestimates some of the topmost cloud range bins. To make up for this, we only use the zenith-pointing lidar's cloud mask, which we refer to as the "relaxed" cloud mask. Furthermore, to reduce possible missing HOIC data points, the non-typed cloud range bins are subjected to further HOIC classification evaluation (i.e., evaluating the ratios of attenuated backscatter and depolarization ratio between the two lidars).

We have carefully tested the dependency of the results to both the relaxed and rigorous cloud masks and found that most findings are robust under both schemes. The main exceptions are the HOIC fraction and the macrophysical characteristics, which will be discussed in detail in the relevant sections below. Since attenuation is common in lidar-based cloud research (Zhao et al., 2014), the relaxed cloud mask better represents the actual cloud structure. Therefore, the relaxed cloud mask is used in this study.

2.3 Duration and horizontal extent of HOIC events

With height-resolved, high-spatiotemporal-resolution cloud phase categorization, the duration and horizontal extent of HOIC events can be estimated. Two HOIC range bins (in the time-height domain) are considered to belong to the same HOIC event if their temporal separation is less than 60 minutes and their vertical separation is less than 2 km ($\Delta t < 60$ min, $\Delta h < 2$ km). A

https://doi.org/10.5194/egusphere-2026-3314
Preprint. Discussion started: 16 June 2026

depth-first search (DFS) algorithm (Cormen et al., 2022) is then applied to group all connected HOIC range bins into individual events.

For each identified HOIC event, the set of unique time indices occupied by the event is extracted. The HOIC event duration is calculated as the number of distinct time steps multiplied by the temporal resolution of 5 minutes. Following the approach of Westbrook et al. (2010), the advection-based horizontal extent of the HOIC event is estimated using horizontal wind speeds interpolated from ERA5 reanalysis data. This quantity should be interpreted as a proxy for horizontal scale rather than a direct geometric cloud width. For each time step belonging to the event, the horizontal displacement is calculated as the wind speed multiplied by the 5-minute time interval. The total geometric extent of the event is obtained by summing these displacements over all time steps of the event. This provides an estimate of the overall horizontal distance over which the HOIC event has been advected during its lifetime.

2.4 Turbulent eddy dissipation rate, HOIC Reynolds number and diameter retrieval

Turbulent eddy dissipation rate (EDR) is retrieved using the cloud radar Doppler velocity together with ERA5 horizontal wind speed. The retrieval method used was compared with the approach proposed by Griesche et al. (2020), showing good agreement in the field experiment on SWC seeding organised by Zhang et al. (2026a). Griesche et al. (2020) retrieved turbulent dissipation rates from cloud radar observations and validated them against tethered-balloon in situ measurements. For HOIC diameter and Reynolds-number estimates, the radar Doppler velocity is treated as the terminal fall velocity, and hexagonal plate assumptions with corresponding mass and area-ratio relationships are used in an aerodynamic model. The technical details are provided in the Appendix of our previous method publication (Wu et al., 2025).

2.5 Statistical Analysis

To quantitatively compare cloud-property distributions for HOICs and ROICs, this study used non-parametric statistical tests. The two-sample Kolmogorov-Smirnov (K-S) test (Massey Jr., 1951) was used to assess whether the two orientation groups originated from the same cumulative distribution, while the Mann-Whitney U test (Mann and Whitney, 1947) was used to evaluate differences in the central tendency (or distribution ranks) of the two groups. Given the exceptionally large sample size in this study, which tends to yield extremely small p-values even for minor physical differences, we further calculated Cliff's Delta (d) to measure the effect size (Cliff, 1993). Effect-size magnitudes follow Romano et al. (2006): negligible for $|d| < 0.147$, small for $0.147 \leq |d| < 0.330$, medium for $0.330 \leq |d| < 0.474$, and large for $|d| \geq 0.474$. All statistical analyses were conducted using the SciPy library in Python (Virtanen et al., 2020).

https://doi.org/10.5194/egusphere-2026-3314
Preprint. Discussion started: 16 June 2026

3 Case studies

To evaluate the proposed cloud-phase categorization method and to investigate the physical mechanisms for the appearance of HOICs, this section presents specific case studies. These cases aim to verify the classification results and to illustrate the strong spatial link between HOICs and overlying SWCs.

3.1 Visual validation of a HOIC event

Figure 1 shows a mid-level cloud case on 14 December 2022, during which strong specular reflections were observed, along with a collocated sun dog photograph. In the zenith-pointing lidar data, the attenuated backscatter is highly enhanced (see the red part in Fig. 1a, from 11:00 to 23:30 local time at the height of 2–4 km). The corresponding volume depolarization ratio approaches near-zero values (blue part in Fig. 1b), which alone would suggest SWCs for those parts of cloud. However, simultaneous observations from the 15° off-zenith pointing lidar reveal a different scenario: in the same region, the attenuated backscatter is notably weaker (in yellow, green and blue of Fig. 1c), and the corresponding volume depolarization ratio is much larger compared to the zenith-pointing lidar (orange and yellow part in Fig. 1d). Consequently, the ratio of attenuated backscatter is quite large (see Fig. 1e) and the ratio of depolarization ratio rather low (see Fig. 1f), meeting the criteria for specular reflection induced by HOICs, instead of SWCs, as introduced in Wu et al., 2025. The categorization result of the cloud phase is shown in Fig. 1g, with HOIC in an orange flag.

A sun dog (parhelion) photograph was captured simultaneously at 16:09 on 14 December 2022 at the Summer Palace in Beijing, approximately 3 km from our lidar station at Peking University (see Fig. 1h). A sun dog is one kind of common atmospheric halo, which requires the existence of horizontally oriented hexagonal plate crystals (Greenler, 1980; Tape, 1994). It exists when the solar elevation angle is low, such as near sunset in this case. Sunlight is refracted twice within the prism facets of these horizontally oriented hexagonal plates to the observer, creating two bright spots besides the sun (Takano and Liou, 1989). In the provided photograph, only the bright spot on the left side of the sun is visible, as the sun itself is outside the frame. A schematic diagram illustrating the formation mechanism of a sun dog is provided in Appendix A.

Given the low solar elevation angle, the exact atmospheric volume producing the observed sun dog may be located at some horizontal distance from our lidar station. Nevertheless, the consecutive orange HOIC label in Fig. 1g means that the horizontal extent of HOIC is very large, likely filling the whole sky. It is highly convincing that HOICs exist above our lidar station. The sun dog photograph serves as independent qualitative evidence to support the validity of our HOIC categorization.

3.2 HOICs under different cloud-top temperatures

Figure 2 presents the cloud phase classification results for representative HOIC cases under various cloud-top temperature (CTT) regimes in 2022. The selected CTTs, ranging from around −15 °C, −25 to −20 °C, −30 to −25 °C, −40 to −25 °C, to < −40 °C, are specifically chosen because they dictate distinct ice crystal growth habits (Bailey and Hallett, 2009). By analyzing these cases, which are primarily stratiform mixed-phase clouds characterized by SWC at the cloud top and ice crystals below,

https://doi.org/10.5194/egusphere-2026-3314
Preprint. Discussion started: 16 June 2026

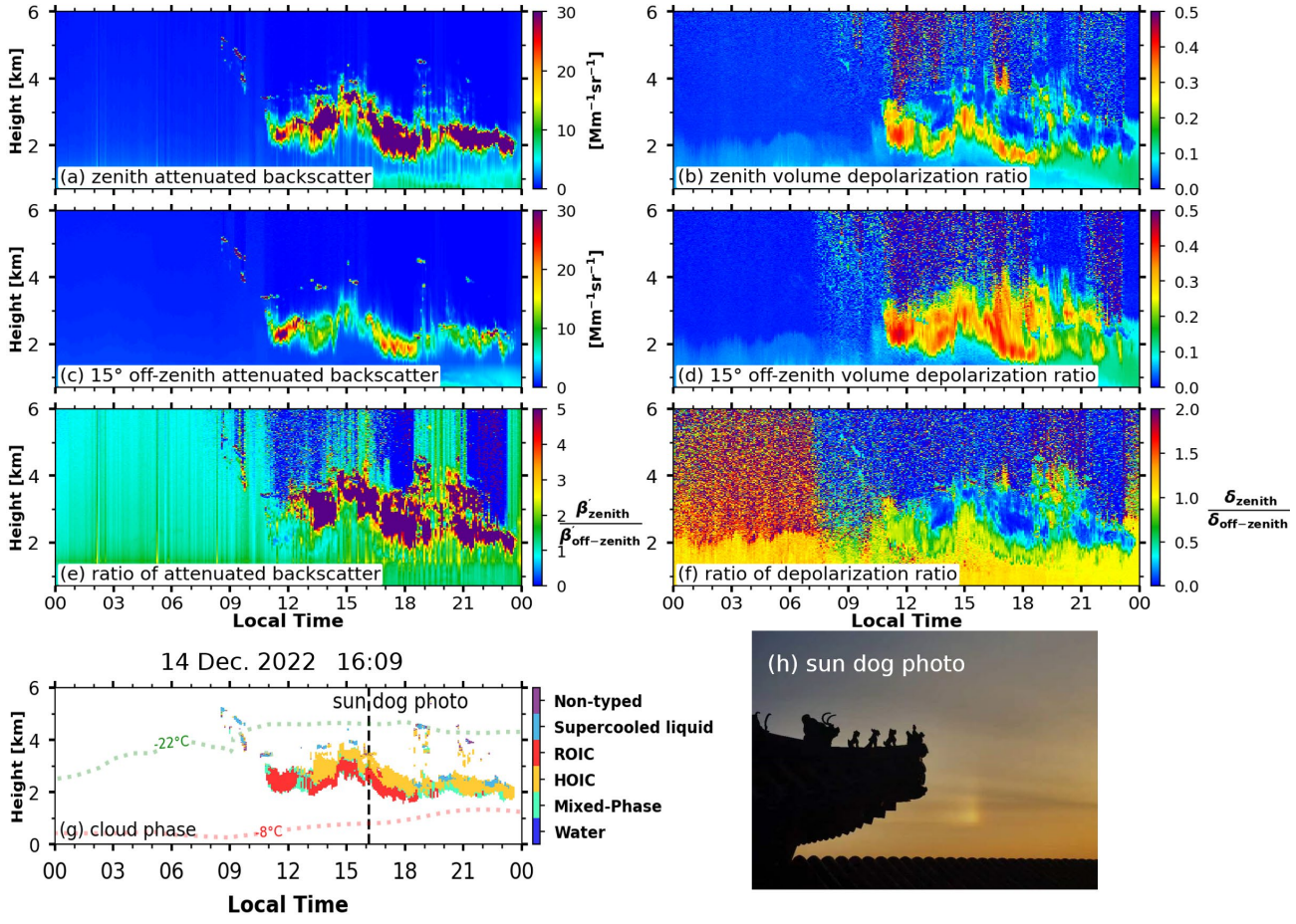

Figure 1. Lidar observations ((a)-(f)), cloud phase categorization (g), and sun dog photo (h) on 14 December 2022 (5 min / 15 m resolution for (a)-(g)). (a) Zenith-pointing lidar attenuated backscatter. (b) Zenith-pointing lidar volume depolarization ratio. (c) 15° off-zenith-pointing lidar attenuated backscatter. (d) 15° off-zenith-pointing volume depolarization ratio. (e) The ratio of attenuated backscatter for zenith-pointing and off-zenith-pointing lidar. (f) The ratio of volume depolarization ratio for zenith-pointing and off-zenith-pointing lidar. (g) Cloud phase categorization results with an isotherm from ERA5 data and a vertical dashed line indicating the sun dog observation time. (h) Sun dog (parhelion) photograph with traditional Chinese-style roof photographed at 16:09, 14 December 2022, approximately 3 km from the lidar station (the Summer Palace, Beijing). Photo courtesy of Hai Feng, used with permission.

this section aims to elucidate a potential relationship between HOICs, crystal growth regime, and the presence of SWCs. SWC, specifically, is a potential candidate to foster the formation of HOIC, because it promotes the growth of simple plate-like crystals rather than irregular polycrystals (Westbrook et al., 2010). Note that while HOIC events with CTTs between −10 °C and −5 °C were also observed in 2022, their vertical structures were overly complex and are therefore not shown here. The corresponding direct observables from the lidars and radar for these cases (e.g., attenuated backscatter, volume depolarization ratio, radar reflectivity, Doppler velocity, spectral width, and EDR) are detailed in Appendix B.

It is important to note that the temperatures discussed here refer specifically to the cloud-top temperatures. As ice crystals sediment after formation, their altitude decreases, and the ambient temperature they experience rises accordingly.

https://doi.org/10.5194/egusphere-2026-3314
Preprint. Discussion started: 16 June 2026

Consequently, the actual temperatures where these ice clouds reside are typically higher than the cloud-top temperatures stated here.

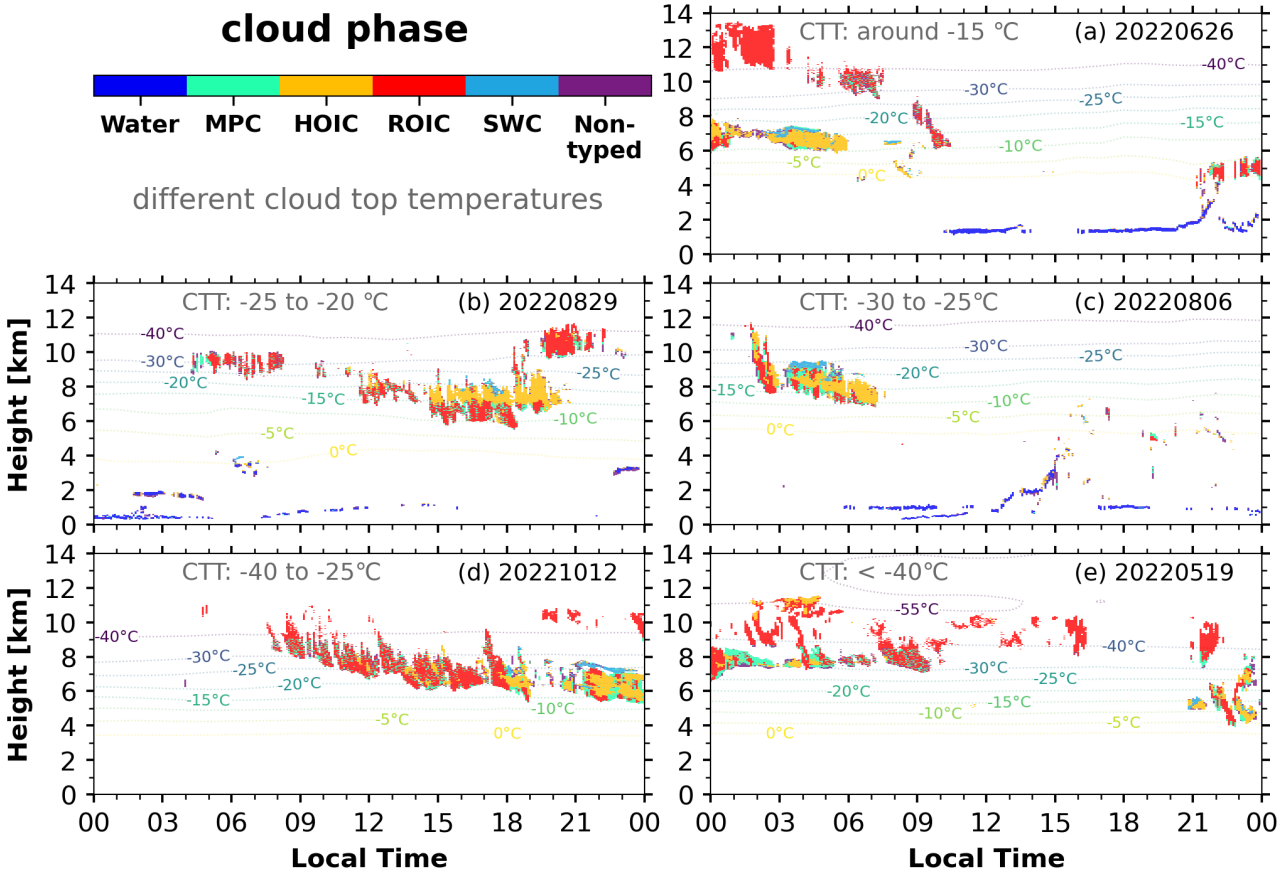

Figure 2. Cloud phase classification plots of horizontally oriented ice crystal (HOIC) cases under different cloud-top temperatures (CTT) across various days in 2022. (a) 26 June 2022 case, CTT around −15 °C; (b) 29 August 2022 case, CTT from −25 °C to −20 °C; (c) 6 August 2022 case, CTT from −30 °C to −25 °C; (d) 12 October 2022 case, CTT from −40 °C to −25 °C; (e) 19 May 2022 case, CTT around −55 °C (below −40 °C). The relaxed cloud mask was used for these classifications.

Figure 2a corresponds to a CTT of approximately −15 °C, which is a typical temperature regime for the formation of plate or dendritic ice crystal habits. From 02:00 to 05:00 on 26 June 2022, a stable layer of SWC existed at the cloud top at an altitude of about 7 km. In this case, HOICs were consistently present at 6–8 km from 00:00 to 06:00. The horizontal orientation of these ice crystals was well maintained between 03:00 and 06:00, with no obvious ROICs appearing at the cloud base.

Figure 2b corresponds to a CTT of approximately −25 to −20 °C, a regime favorable for the plate-like ice crystal formation. On 29 August 2022, between 17:00 and 18:00, an SWC layer was present at the cloud top at an altitude of about 8 km. In this case, stable HOICs were consistently present at 7–9 km from 15:00 to 21:00, corresponding to ambient temperatures of −20 to −15 °C. Between 15:00 and 18:00, the horizontal orientation of ice crystals at 6–7 km could not be maintained in the lower portions, resulting in the appearance of a massive amount of ROIC forming a layer up to 1 km thick.

https://doi.org/10.5194/egusphere-2026-3314
Preprint. Discussion started: 16 June 2026

Figure 2c corresponds to a CTT of approximately −30 to −25 °C, a regime favorable for polycrystalline plate ice-crystal formation. On 6 August 2022, from 03:00 to 05:00, a stable SWC layer existed at the cloud top at approximately 9 km. In this case, stable HOICs were consistently present at 7–9 km from 03:00 to 07:00, corresponding to temperatures of −20 to −10 °C. At the cloud base, the horizontal orientation was not fully maintained, and ROICs occurred.

Figure 2d presents a typical case illustrating the relationship between supercooled liquid water and HOIC. On 12 October 2022, a cloud layer was observed around 08:00. Initially, the cloud-top temperature was low, with values below −40 °C. Subsequently, the cloud layer's altitude gradually decreased, and its temperature gradually increased. As the cloud-top temperature reached approximately −30 °C (around 12:00), a distinct region of HOIC became evident. When the cloud-top altitude further decreased, with the cloud-top temperature rising to approximately −25 °C (around 18:00), supercooled liquid water (marked in light blue) appeared at the cloud top, and the number of HOIC range bins began to multiply. After 21:00, the cloud-top temperature was around −25 °C, and a stable SWC top emerged; the HOIC increased significantly and began to dominate the entire cloud layer. The presence of SWCs led to a rapid increase in HOIC occurrence. This case fully demonstrates that the presence of SWCs is a favorable condition for the occurrence of HOICs.

Figure 2e presents a case of a pure cirrus cloud without the presence of SWCs. On 19 May 2022, the CTT was below −55 °C, which is significantly lower than the homogeneous freezing threshold (−38 °C). At this temperature, supercooled liquid water cannot exist, and the cloud must be entirely composed of ice crystals. From 03:00 to 05:00, significant signals of HOICs were observed at the cloud top at an altitude of 11 km, persisting for nearly two hours. This case demonstrates that HOICs can also occur in cirrus clouds without supercooled liquid water above.

Note that the corresponding raw observational quantities from the lidar and cloud radar for the aforementioned cases shown in Fig. 2, including attenuated backscatter, volume depolarization ratio, radar reflectivity factor, Doppler velocity, spectral width, and EDR, are detailed in Appendix B.

4 Statistical results

This section presents the year-long statistical results of HOICs derived from the 2022 observations. We first examine the bulk statistical characteristics of the direct observables from the dual-angle lidars, including attenuated backscatter and volume depolarization ratio, in order to illustrate the fundamental optical signatures of HOICs. We then move on to the statistical characteristics of the retrieved products, followed by analyses of their diurnal variation, environmental dependencies, and radar-based dynamical and microphysical properties.

4.1 Bulk statistics of Direct Observables

Figure 3 shows the temperature dependence of the statistical characteristics of the volume depolarization ratio and attenuated backscatter for cloud data points observed by the lidars in 2022. In Fig. 3a, the volume depolarization ratio distributions from the zenith-pointing (blue) and 15° off-zenith (gray) lidars are compared by temperature bin. The figure marks the median

https://doi.org/10.5194/egusphere-2026-3314
Preprint. Discussion started: 16 June 2026

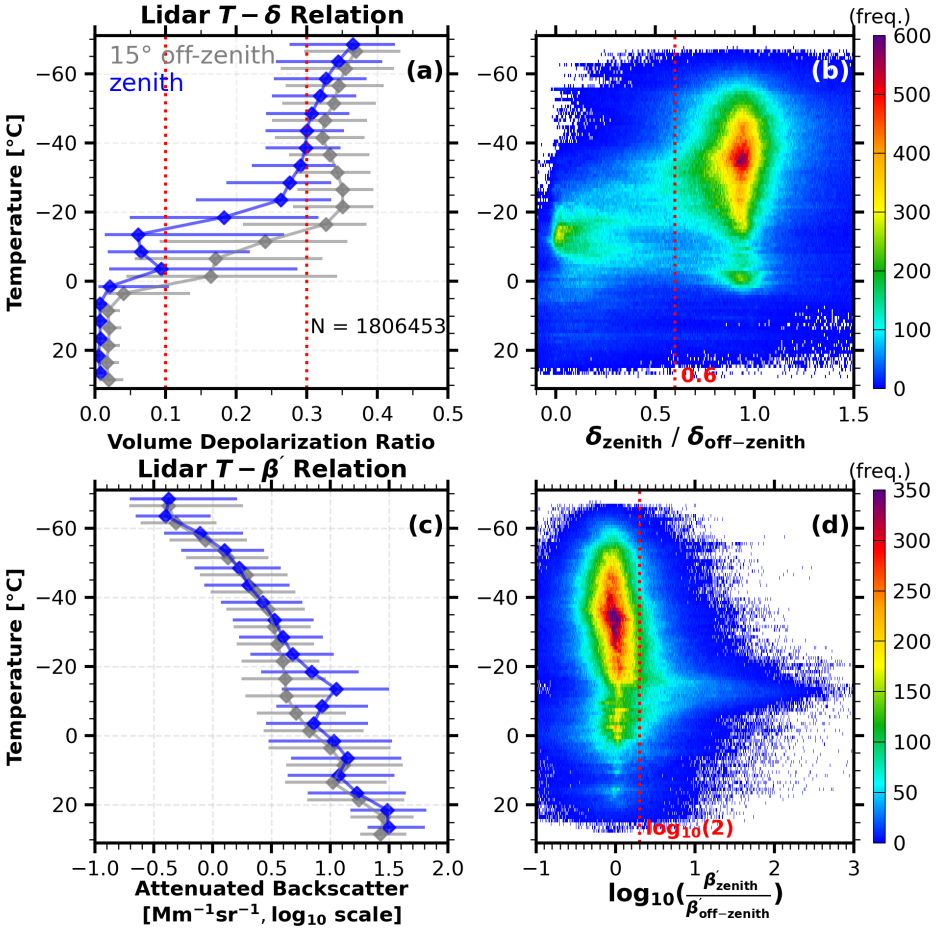

Figure 3. Lidar measurements across different temperature intervals: (a) zenith and off-zenith volume depolarization ratios; (b) the zenith-to-off-zenith ratios of volume depolarization; (c) zenith and off-zenith attenuated backscatter; (d) the zenith-to-off-zenith ratios of attenuated backscatter (on a base-10 logarithmic scale). In (a) and (c), the diamond markers represent the median of the data within each 5 °C temperature bin, and the horizontal error bars span the interquartile (25th–75th percentile) range. All identified cloud data points from 2022 are used in these plots.

(diamonds) and interquartile range (horizontal lines) for each temperature interval. Below −40 °C and above 0 °C, the two lidars give broadly consistent depolarization ratios. However, in the mixed-phase cloud temperature range from −40 °C to 0 °C, the off-zenith depolarization ratios are distinctly higher than the zenith-pointing values. The largest median difference, about 0.18, occurs between −15 and −10 °C. The −20 °C to −15 °C interval exhibits the second-highest difference, with values reaching 0.15. These pronounced discrepancies are a clear signature of HOICs, which cause a strong reduction in the zenith-pointing lidar depolarization ratio due to specular reflection.

Note that in liquid water clouds at temperatures above 0 °C, the off-zenith lidar depolarization ratio is slightly higher. This difference is primarily explained by the different fields of view (FOV) of the two instruments. The off-zenith AVORS lidar has a larger FOV (0.2 mrad) than the zenith lidar (0.1 mrad), making it more sensitive to multiple scattering effects, which in

https://doi.org/10.5194/egusphere-2026-3314
Preprint. Discussion started: 16 June 2026

turn increase the measured depolarization ratio (Jimenez et al., 2020b). At temperatures below −40 °C, the off-zenith lidar depolarization ratio is slightly higher likely due to a small presence of HOICs.

Figure 3b presents a density scatter plot showing the ratio of the depolarization ratios ($\delta_{\text{zenith}}/\delta_{\text{off-zenith}}$) from the two lidars against temperature. The vast majority of data points, corresponding to ROICs and to liquid-water droplets, cluster around a ratio of 1 (the red, yellow, and green high-density areas). However, between −20 °C and −10 °C, a distinct yellow-green data cluster emerges, indicating the presence of HOICs, corresponding to a ratio close to 0.

The vertical red dashed line in the figure marks the threshold of 0.6 used in the identification algorithm of this study (Wu et al., 2025). The density scatter distribution confirms the physical validity of this threshold: it effectively isolates data where the zenith-pointing depolarization ratio is significantly lower than the off-zenith one (i.e., HOIC-dominated regions), while successfully excluding the majority of conventional cloud data (with a ratio near 1) from being misidentified.

The attenuated-backscatter statistics in Fig. 3c show a complementary pattern. In most temperature ranges, the two lidars measure similar attenuated backscatter values. Between −20 and 0 °C, however, zenith-pointing attenuated backscatter is enhanced relative to the off-zenith signal, again indicating specular reflection. In the −15 to −10 °C temperature interval, the zenith median attenuated backscatter is nearly half an order of magnitude larger than the off-zenith median, representing a substantial discrepancy.

Figure 3d is a density scatter plot showing the base-10 logarithmic ratio of the attenuated backscatter from the two lidars as a function of temperature. The vast majority of data points in the figure are concentrated around 0 (i.e., a linear ratio of approximately 1), indicating that for most cloud data points, the backscatter intensities received by the two lidars are comparable, with no significant specular reflection. However, between −20 °C and 0 °C, a “spike-like” dense cluster of data points clearly extends to the right. This represents a strong specular reflection region where the signal intensity of the zenith-pointing lidar far exceeds that of the off-zenith lidar. Particularly in the −15 °C to −10 °C interval, the difference between the two reaches its maximum; the attenuated backscatter coefficient of the zenith-pointing lidar can be up to 3 orders of magnitude higher than that of the off-zenith-pointing lidar (i.e., the base-10 logarithmic ratio reaches 3).

The vertical red dashed line in the figure marks the threshold used in the identification algorithm, corresponding to a linear ratio of 2. The density scatter distribution confirms the physical validity of this threshold selection: the algorithm selectively isolates data where the zenith-pointing scattering intensity is significantly higher than the off-zenith one (ratio > 2), while successfully excluding the conventional scattering cloud data points where the ratio is close to 1 (indicated by the red, yellow, and green colors).

Figure 4 displays the joint two-dimensional frequency distributions of the volume depolarization ratio (δ) and the logarithmic attenuated backscatter for both the zenith-pointing and off-zenith-pointing lidars across different temperature intervals, along with the characteristics of their density differences. This figure compiles valid cloud data points for the entire year of 2022. Distinct cloud microphysical phases occupy different regions in the joint distribution diagrams. Liquid water clouds, consisting of high concentrations of spherical water droplets, exhibit low (near-zero) depolarization ratios and high

https://doi.org/10.5194/egusphere-2026-3314
Preprint. Discussion started: 16 June 2026

attenuated backscatter coefficients (Hamel et al., 2026). Conventional ice clouds (ROICs), dominated by non-spherical ice crystals with relatively lower number concentrations, show high depolarization ratios and low-to-moderate attenuated backscatter. The black dashed boxes in the lower right corners of Figs. 4a and 4b indicate the threshold range to identify liquid water clouds introduced in Wu et al. (2025): $\delta_v < 0.1$ and $\beta' > 5$ Mm^{-1} sr^{-1} (attenuated backscatter coefficient).

It should be noted that the algorithm used in this study requires the depolarization ratio of HOICs observed by the zenith-pointing lidar to be below 0.1. However, in practice, this study selected only the most representative HOICs. Some range bins contain HOICs at relatively low concentrations, resulting in depolarization ratios with values that are lower than those of ROICs but may still exceed the 0.1 threshold.

First, the warm cloud regime with $T > 0$ °C is evaluated. When the temperature exceeds 0 °C (Figs. 4a1 and 4b1), clouds consist primarily of warm liquid water. The high-density data points from both lidars fall precisely into the dashed box in the lower right corner, confirming the physical validity of the liquid water cloud thresholds defined in this study. The few data points scattered outside the box mainly arise from large, falling ice crystals that have not fully melted or from aerosol particles misidentified as clouds. When the temperature exceeds 3–5 °C (not shown), the remaining ice-phase particles finally melt, and nearly all cloud data points become concentrated within the dashed box in the lower right corner.

A careful comparison between Figs. 4a1 and 4b1 reveals that the data points from the zenith-pointing lidar lie closer to the x-axis (where the depolarization ratio is near zero). This difference arises from the larger field of view of the off-zenith lidar, which enhances multiple-scattering effects and slightly increases depolarization in dense water clouds (Jimenez et al., 2020a).

Second, the pure ice cloud regime of temperatures ≤ −38 °C is discussed in detail. When the temperature drops below the homogeneous nucleation threshold of −38 °C, the clouds are composed entirely of the ice phase. All supercooled liquid water freezes, and no SWCs can exist within this temperature regime (Pruppacher and Klett, 2010). Figure 4b4 shows that all cloud data points observed by the off-zenith lidar exhibit high depolarization ratios and low backscatter, perfectly clustering in the upper-left ice cloud region outside the dashed box. This further proves the robustness of the liquid water threshold established in Wu et al. (2025). Conversely, in the zenith-pointing observations (Fig. 4a4), a small number of data points still fall within the dashed box, suggesting some presence of HOICs even at these low temperatures.

Third, the mixed-phase cloud regime (−38 °C < T ≤ 0 °C) is discussed. This temperature regime is an active zone for ice-water phase transitions and the frequent occurrence of HOICs. In the −20 °C to 0 °C interval, the cloud parameter space clearly splits into two distinct extremes: a conventional ice cloud region in the upper-left part and a liquid-water-like cloud cluster in the lower-right part. Comparing of Figs. 4a2 and 4b2 indicates that the zenith-pointing lidar accumulates a very large cluster of data points in the lower-right part. This difference is more intuitively illustrated in Fig. 4c2 (off-zenith minus zenith density), where negative values prevail in the lower-right part (zenith density > off-zenith density), whereas positive values prevail in the upper-left part (off-zenith density > zenith density). In other words, when the lidar observation switches from zenith to off-zenith probing, a large number of data points originally concentrated in the low-depolarization-ratio, high-backscatter region migrate in the parameter space and return to their background ice cloud location, which is characterised by a high

https://doi.org/10.5194/egusphere-2026-3314
Preprint. Discussion started: 16 June 2026

335 depolarization ratio and lower backscatter. These particles, which thus reveal their true non-spherical morphology, are precisely the HOICs responsible for the strong zenith reflections.

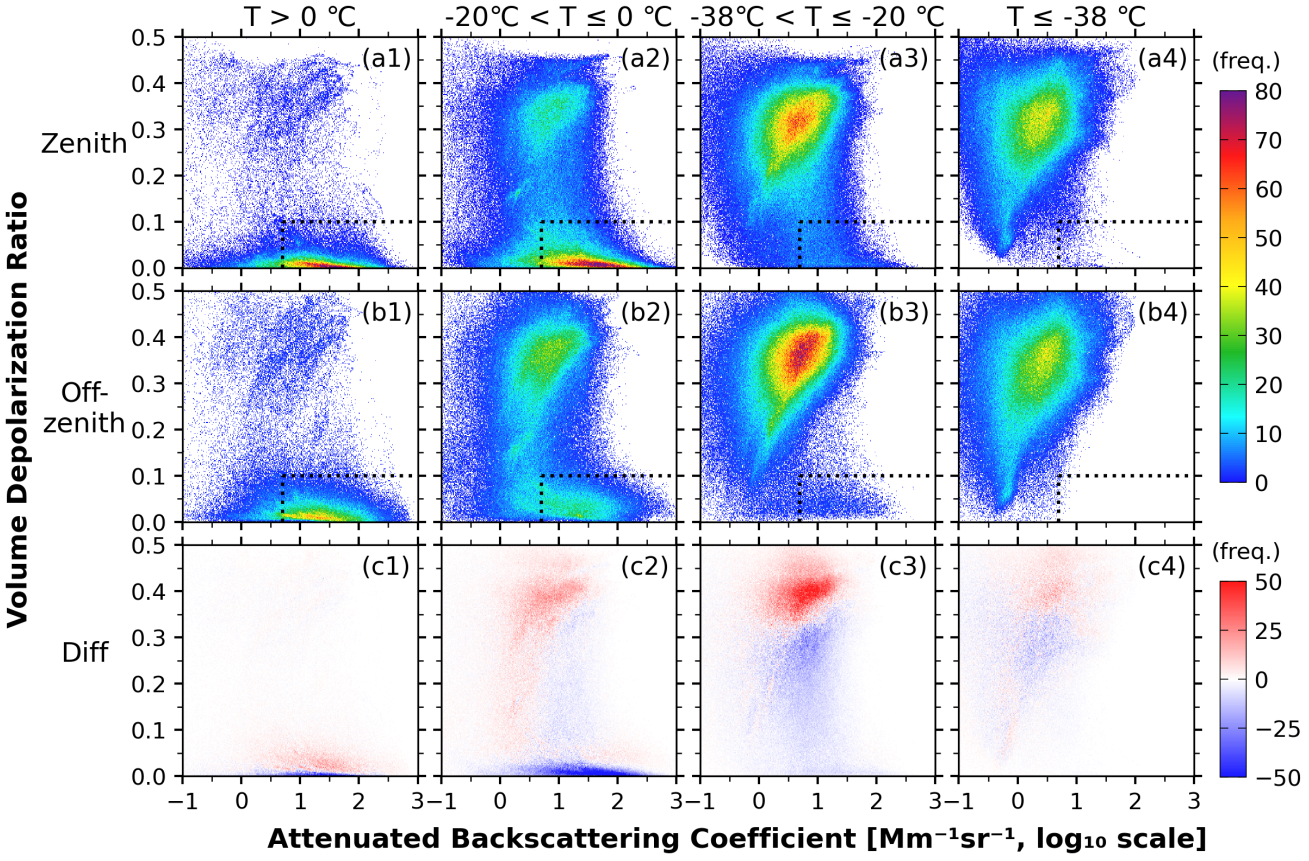

Figure 4. Volume depolarization ratio versus attenuated backscatter ($\log_{10}$ scale) density scatter plots across different temperature intervals for: (a) zenith-pointing lidar; (b) off-zenith pointing lidar; and (c) the density difference between off-zenith and zenith
340 **measurements. Data points are shown in blue where the zenith scatter density exceeds the off-zenith density, and in red where the off-zenith density is higher. Panels correspond to the following temperature regimes: (1) $T > 0$ °C; (2) −20 °C < $T \leq 0$ °C; (3) −38 °C < $T \leq -20$ °C; and (4) $T \leq -38$ °C. The liquid-water-cloud identification threshold is marked by the black dashed line at lower right (see Wu et al., 2025, Fig. 3c). This figure includes all cloud data points measured in 2022. During the gridding process, the resolutions for the $\log_{10} \beta'$ and δ were set to 0.01 and 0.2%, respectively.**

345 In the −38 °C to −20 °C interval (Figs. 4a3–4b3), the bimodal distribution persists. The difference map (Fig. 4c3) shows that the low-depolarization region (δ between 0 and 0.3) is dominated by negative values (higher frequency in zenith observations), whereas the high-depolarization region centred near $\delta \approx 0.4$ is dominated by positive values (higher frequency in off-zenith observations). This indicates that within this temperature regime, some range bins are still mixed with HOICs, and their presence biases the depolarization ratio observed by the zenith lidar towards lower values. However, compared with the −20 °C
350 to 0 °C interval, the frequency difference within the dashed box is no longer significant. The primary difference area is located

https://doi.org/10.5194/egusphere-2026-3314
Preprint. Discussion started: 16 June 2026

in the upper left part of the dashed box, indicating that the occurrence frequency of HOICs decreases markedly in this temperature regime.

4.2 Bulk statistics of Retrieved Products

While Section 4.1 focuses on the direct optical signatures measured by the lidars, this subsection examines the statistical characteristics of the retrieved cloud-phase products. We begin with the occurrence frequency and cloud-phase fractions, followed by the macrophysical and spatiotemporal characteristics of HOIC events.

4.2.1 Occurrence frequency and cloud-phase fractions

Figure 5 presents the overall and seasonal distributions of cloud phases in the Beijing area for the year 2022, shown as pie charts (Fig. 5a, b), together with radiosonde temperature profiles from Beijing Nanjiao Meteorological Observatory (WMO no. 54511, Fig. 5c). The "Total Cloud Phase" category includes the six types defined in our classification scheme (Wu et al., 2025): HOIC, ROIC, mixed-phase cloud (MPC), SWC, warm water cloud (Water), and unclassified data (Non-typed). The term "Ice-containing" refers specifically to the subset consisting of HOIC, ROIC, and MPC, all of which contain ice particles. This study focuses on the statistical analysis of the HOIC proportion within both the total cloud phase and the ice-containing cloud categories.

As shown in Fig. 5a, the number of valid data points for the total cloud phase throughout 2022 exceeds 2.5 million, ensuring sufficient statistical significance. Among total cloud phases, the fraction of HOICs is 12.3%, which is notably higher than that of SWCs (4.3%) and warm water clouds (5.2%). ROICs account for the largest share of the observed cloud data points, exceeding half of the total. Further analysis of the annual ice-containing cloud data points (Fig. 5b, with a sample size exceeding 2 million) reveals that the fraction of HOICs reaches 15.0%, while ROICs approaches 70.0%. This indicates that HOICs constitute a non-negligible proportion within natural ice clouds. However, it should be noted that these fractions are calculated from lidar-resolved cloud data points. Ice-containing clouds often have a larger vertical extent, whereas stratiform liquid-water clouds are typically shallower, and deep liquid-cloud layers may also be partly underrepresented because of strong lidar attenuation.

Figures 5a1–a4 and 5b1–b4 present the cloud phase classification results for all clouds and ice-containing clouds in four different seasons, respectively. Statistical analysis reveals significant seasonal variations in the occurrence frequency of HOIC. Within the ice-containing clouds during summer (JJA) and autumn (SON), the fractions of HOIC are as high as 24.6% and 20.5%, respectively; whereas in winter (DJF) and spring (MAM), these fractions drop to 8.2% and 9.8%, respectively.

https://doi.org/10.5194/egusphere-2026-3314
Preprint. Discussion started: 16 June 2026

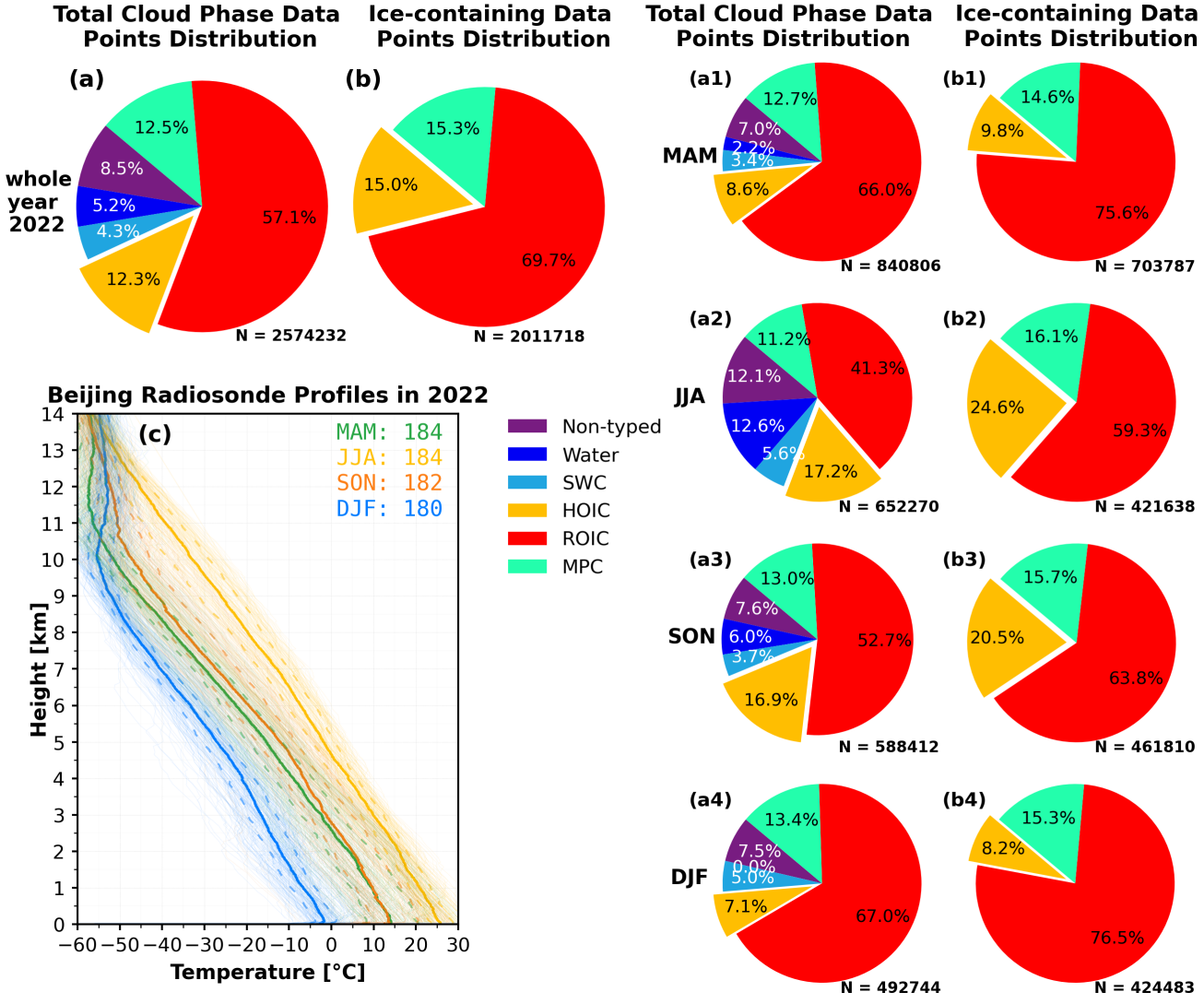

Figure 5. Statistical characteristics of cloud phase distributions and radiosonde profiles in Beijing for 2022: (a) Cloud phase distribution pie charts of all cloud data points annually and by season (a1)–(a4). (b) Cloud phase distribution pie charts of ice-containing cloud data points annually and by season (b1)–(b4), with HOIC highlighted in orange. (c) Seasonal radiosonde profiles from Beijing station (WMO no. 54511) in 2022 (light background lines: individual profiles; solid lines: medians; dashed lines: median ± one standard deviation). MAM, JJA, SON, and DJF denote spring (March–May), summer (June–August), autumn (September–November), and winter (December–February), respectively. Cloud-phase statistics in this figure are based on the relaxed cloud mask. Abbreviations: Water (warm water cloud), SWC (supercooled liquid water cloud), HOIC (horizontally oriented ice crystal), ROIC (randomly oriented ice crystal), MPC (mixed-phase cloud).

These seasonal differences can be explained by analyzing the seasonal radiosonde temperature profiles from the Beijing Nanjiao Meteorological Observatory (Fig. 5c). Based on the temperature characteristic analyses in Sects. 4.1 and the subsequent Sect. 4.4, HOICs tend to form in the temperature regime around −15 °C. As shown in Fig. 5c, the −15 °C isotherm in Beijing during summer is located at an altitude of approximately 7 km. This altitude corresponds to the region where mid-

https://doi.org/10.5194/egusphere-2026-3314
Preprint. Discussion started: 16 June 2026

level clouds frequently occur, providing ample physical space for the formation of HOICs. In contrast, the average surface temperature in winter is below 0 °C, and the −15 °C isotherm drops to approximately 2 km. Observational experience indicates that clouds appear much less frequently at an altitude of 2 km compared to 7 km, which is also confirmed by CALIPSO (Cloud-Aerosol Lidar and Infrared Pathfinder Satellite Observations) observations (Pan et al., 2016; Chi et al., 2022). Even when clouds are present at this lower altitude around 2 km, they are predominantly boundary-layer liquid water clouds rather than ice clouds. Moreover, the cloud identification algorithm in this study has already filtered out low-altitude precipitation signals. Consequently, the lower altitude of the −15 °C isotherm in winter is unfavorable for the widespread generation of HOICs.

Similarly, the radiosonde data indicate that the overall temperature profile in spring is lower than in autumn, more closely resembling winter conditions, whereas the autumn profile is closer to summer conditions. This may explain why the occurrence frequency of HOICs in spring (9.8%) is substantially lower than that in autumn (20.5%). Furthermore, the tendency for horizontal orientation may inherently vary with altitude. At lower altitudes, where air density is higher, increased aerodynamic drag could enhance local turbulence, thereby hindering the stable horizontal orientation of ice crystals.

It is noteworthy that the fraction of HOICs in summer ice-containing clouds reaches 24.6%. Such a high frequency of occurrence demands sufficient attention. Some previous studies relying solely on zenith-pointing lidars for cloud phase identification have ignored the presence of HOICs, simply misidentifying all signals exhibiting high backscatter and low depolarization characteristics as SWCs (Wang et al., 2022). Benefiting from the range-bin-by-range-bin products of HOICs and SWCs obtained in this study, the following quantitatively evaluates the impact of this misidentification.

If the presence of HOICs were ignored and the 12.3% of HOICs were all misidentified as SWCs, then true SWCs would actually only account for 4.3% / (12.3% + 4.3%)≈ 25.9%. In other words, the potential misidentification rate would be as high as 12.3% / (12.3% + 4.3%) ≈ 74.1%—meaning that over 70% of these data points are actually HOICs rather than SWCs. Note that if we use the rigorous cloud mask which tends to underestimate the HOIC fraction, the fractions of SWCs and HOICs among total cloud data points are 4.7% and 6.3%, respectively (Wu et al., 2026). The corresponding misidentification rate is still 6.3% / (4.7% + 6.3%)≈57%. This misidentification of HOICs as SWCs is prevalent in the existing literature (Wang et al., 2022; Whitehead et al., 2024), indicating that the amount of HOICs has been largely underestimated in previous studies.

4.2.2 Macrophysical and spatiotemporal characteristics

To further investigate the macrophysical properties of HOICs, we examined their duration (the time period over which clouds pass above the station) and horizontal extent. Here, the horizontal extent is derived by multiplying the cloud duration by the horizontal wind speed, which serves as a proxy for the spatial scale of the cloud. It should be noted that while the observed duration is statistically correlated with the overall cloud lifetime, it specifically represents the transit time across our observation site rather than the entire lifecycle of the cloud. The detailed methods used to derive these quantities are described in Sec. 2.3. Given that the statistical characteristics are sensitive to the threshold choice in the cloud identification algorithm, we conducted a comparative analysis using both “rigorous” and "relaxed" cloud identification schemes.

https://doi.org/10.5194/egusphere-2026-3314
Preprint. Discussion started: 16 June 2026

First, we evaluate the rigorous cloud identification scheme. Figure 6 presents the statistical results for the duration and horizontal extent of HOICs derived from the rigorous method. Applying the aforementioned event merging criteria ($\Delta t < 60$ min, $\Delta h < 2$ km) yielded a dataset of 735 HOIC events in 2022.

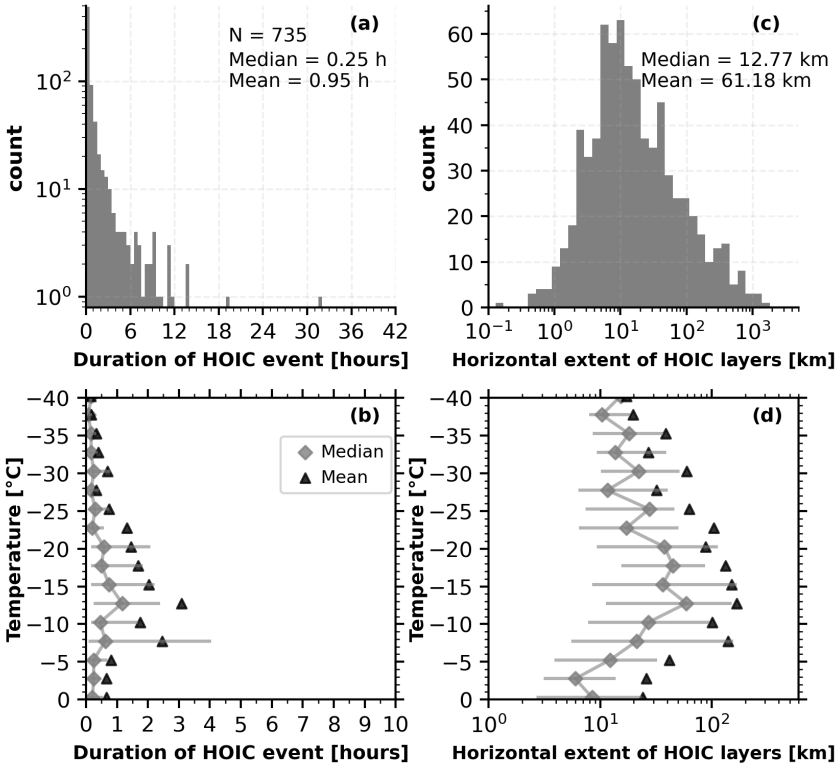

Figure 6. Duration and horizontal extent of HOICs using the rigorous cloud mask. Overall, the durations and horizontal scales are smaller than those obtained using the relaxed cloud mask. Panels show: (a) frequency histogram of HOIC duration; (b) distribution of HOIC duration across temperature intervals (2.5 °C bins), where diamonds denote medians, triangles denote means, and horizontal lines cover the 25th to 75th percentile range; (c) frequency histogram of HOIC horizontal extent; (d) distribution of HOIC horizontal extent across temperature intervals (2.5 °C bins).

As shown in the frequency histogram in Fig. 6a, most HOIC events have relatively short durations, concentrated within 12 h (only three events exceeding 12 h), with a median of 0.25 h and a mean of 0.95 h. Figure 6b presents the distribution of HOIC durations across different temperature regimes. The analysis reveals that the HOIC duration is longest within the temperature interval of −25 °C to −5 °C, peaking specifically in the −15 °C to −10 °C interval.

Figure 6c shows that the horizontal extent of these events exhibits an approximately log-normal distribution, roughly varying between 1 and 1000 km, peaking at the order of 10 km. The median horizontal length is 12.77 km and the mean is 61.18 km, indicating that the macroscopic horizontal scale of a typical HOIC event is roughly on the order of 10 to 100 km. Regarding its temperature dependence (Fig. 6d), the horizontal extent reaches its maximum within the −25 °C to −5 °C regime, with a pronounced peak particularly around the −20 °C to −10 °C interval, but this is also the temperature range where most of the HOIC events occurred.

https://doi.org/10.5194/egusphere-2026-3314
Preprint. Discussion started: 16 June 2026

For comparison, Figure 7 presents the statistical results based on the relaxed cloud identification method. Under this criterion, a total of 693 HOIC events were identified throughout the year. The relaxed cloud identification method captures a more complete cloud life cycle, resulting in substantial increases in both the derived duration and horizontal extent. Figure 7a shows that although the events are still predominantly short-lived, the median and mean durations have increased to 0.33 h and 1.97 h, respectively (with three events exceeding a duration of 24 h). Figure 7b illustrates the distribution of HOIC durations across different temperature regimes. Consistent with the rigorous method, the HOIC duration under the relaxed method is also longest in the −25 °C to −5 °C interval, peaking between −15 °C and −10 °C. This consistency verifies the robustness of the statistical results.

Similarly, the median horizontal extent (Fig. 7c) is 17.76 km, while the mean increases to 112.77 km. Regarding the temperature distribution characteristics (Fig. 7d), the high-value region under the relaxed method remains between −25 °C and −5 °C. Notably, within the core temperature regime of −18 °C to −10 °C, the mean horizontal scale of the HOIC cloud layers generally exceeds 100 km.

A comprehensive comparison of the two schemes, together with consideration of the severe attenuation encountered by the off-zenith AVORS lidar when penetrating cloud layers, indicates that the relaxed cloud identification method better captures the true cloud boundaries. Consequently, its statistical results are closer to the actual physical state of HOICs. Overall, typical HOIC layers exhibit the following macrophysical characteristics. HOIC event duration is longest in the −20 °C to −10 °C regime, where they can persist for several hours, whereas in other temperature ranges the average duration is less than 1 h. HOIC event horizontal scale is predominantly on the order of 10 to 100 km, which corresponds to a typical mesoscale meteorological feature. Within the optimal HOIC growth regime of −20 °C to −10 °C, however, the mean horizontal scale can extend beyond 100 km.

These statistical results hold significant physical meaning and show good agreement with earlier observational studies. For example, He et al. (2021) manually identified 32 HOIC events over Wuhan by visual inspection, and reported that the horizontal orientation was sustained for 0.3 to 8.5 h, averaging 3.5 h. The mean duration obtained in this study under the relaxed method (1.97 h) is on the same order of magnitude as their result. The discrepancy may stem from the different event truncation criteria between the automated algorithm and manual subjective identification, as well as the significantly expanded sample size in this study (693 events). Regarding the horizontal scale, Westbrook et al. (2010) estimated the mean scale of HOICs in mid-level clouds to be approximately 15 km, and around 5 km at −35 °C. The median horizontal scale calculated in this study (12.77–17.76 km) closely matches the estimate reported by Westbrook et al. (2010). Furthermore, the larger mean scale (> 100 km) detected in the most suitable temperature regime further confirms that expansive stratiform cloud systems serve as excellent host environments for HOIC formation.

https://doi.org/10.5194/egusphere-2026-3314
Preprint. Discussion started: 16 June 2026

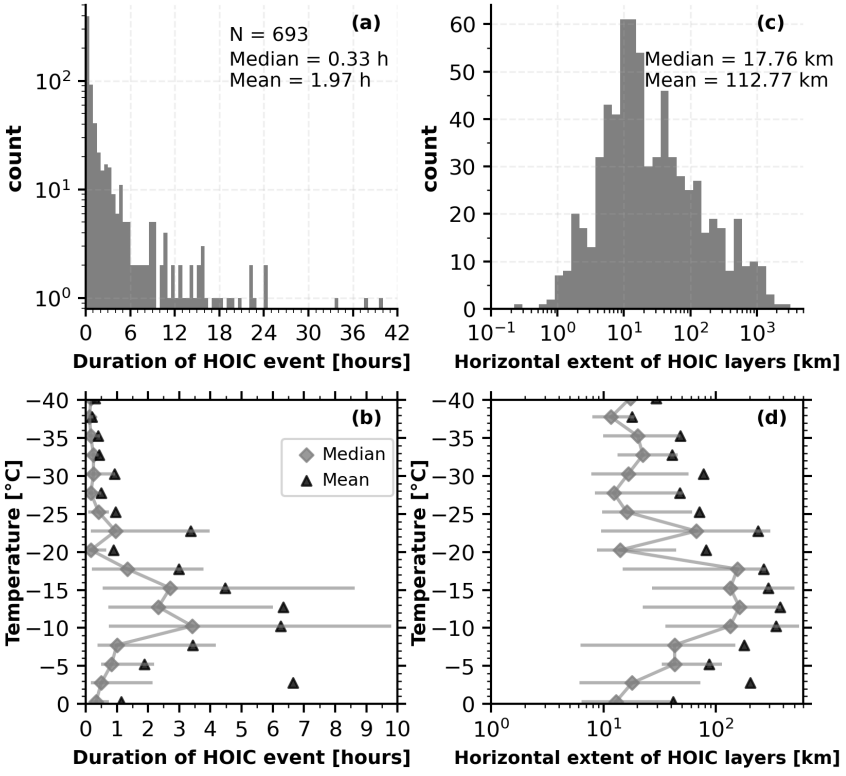

Figure 7. Duration and horizontal extent of HOICs using the relaxed cloud mask. Overall, the durations and horizontal scales are larger than those obtained using the rigorous cloud mask. Panels show: (a) frequency histogram of HOIC duration; (b) distribution of HOIC duration across temperature intervals (2.5 °C bins), where diamonds denote medians, triangles denote means, and horizontal lines cover the 25th to 75th percentile range; (c) frequency histogram of HOIC horizontal extent; (d) distribution of HOIC horizontal extent across temperature intervals (2.5 °C bins).

4.3 Diurnal variability

Figure 8 shows the two-dimensional local-time-temperature distributions of cloud mean attenuated backscatter coefficient (β') and depolarization ratio (δ) measured by the lidars at different pointing angles. The sampling intervals for time and temperature are 0.5 hours and 1 °C, respectively. Overall, the spatiotemporal distributions of both lidar parameters exhibit significant temperature and temporal dependencies.

One of the most prominent features in Fig. 8 is the presence of a distinct low-δ layer near −15 °C, which is generally attributed to signals originating from HOICs. This low-δ layer is particularly pronounced in the zenith-pointing lidar observations (Fig. 8a1), where the corresponding β' values are anomalously high (> 10 $\mathrm{Mm^{-1}sr^{-1}}$; see Fig. 8b1, note that the figure uses a $\log_{10}$ scale). This is caused by specular reflection during zenith pointing. In the warm cloud regime with temperatures above 0 °C, extremely high backscatter and extremely low depolarization ratios are also observed. However, these features arise from the high number concentration and spherical shape of liquid water droplets, a mechanism fundamentally different from the specular reflection of ice crystals.

https://doi.org/10.5194/egusphere-2026-3314
Preprint. Discussion started: 16 June 2026

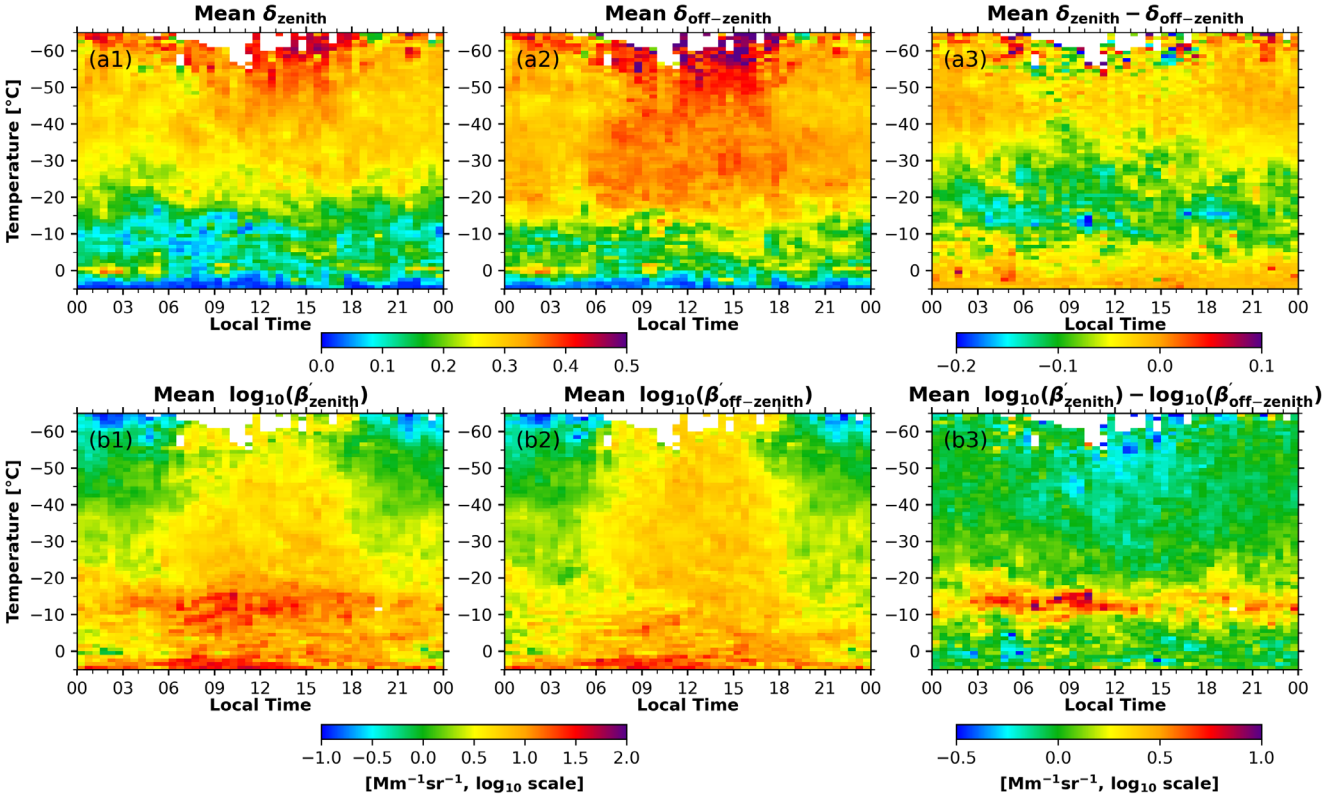

Figure 8. Local time versus temperature cross-sections of the mean values of: (a) volume depolarization ratio and (b) attenuated backscatter ($\log_{10}$ scale). Panels correspond to (1) zenith-pointing lidar, (2) off-zenith pointing lidar, and (3) the difference between the zenith and off-zenith measurements.

When observing with an off-zenith pointing lidar (Fig. 8a2), the δ values detected near −15 °C are higher because the specular reflection angle of HOIC is avoided. Simultaneously, the corresponding β' values drop noticeably (Fig. 8b2). Figure 8a3 shows the difference in depolarization ratio between the zenith and off-zenith pointing lidars. A substantial difference between the two occurs in the temperature interval of −30 °C to −10 °C, peaking around −15 °C. Figure 8b3 shows the difference in attenuated backscatter between the zenith and off-zenith pointing lidars, again revealing a substantial difference between −20 °C and −10 °C.

Regarding diurnal variations, observations show that at temperatures below −20 °C, the cloud backscatter detected during the daytime is generally stronger than at night, with correspondingly higher depolarization ratios. As seen in Figure 8a3, the diurnal variation of the depolarization ratio difference is generally weak, with minimum values at 10:00–11:00 and 16:00–20:00 (which correspond to higher differences in attenuated backscatter). However, the lidar cloud detection algorithm can be affected by solar background noise during daytime (Zhao et al., 2014), resulting in a lower SNR that may cause only optically thick clouds with sufficiently strong signals to trigger the cloud identification algorithm. The conclusions of this study may be subject to such lidar instrument-related limitations. We have attempted to remove cloud data points detected at nighttime

https://doi.org/10.5194/egusphere-2026-3314
Preprint. Discussion started: 16 June 2026

whose attenuated backscatter was lower than the minimum attenuated backscatter of clouds detected during the daytime by using the daytime minimum as a threshold. A figure with a similar pattern to Fig. 8 was generated based on this approach (figure not shown), and the resulting day-night distribution showed no significant difference. Finally, we present the current diurnal variations here.

It is worth noting that Kikuchi et al. (2021) utilized data from the spaceborne CALIOP lidar at different pointing angles, finding a similar latitude-temperature distribution (see Fig. 2 in their paper). However, constrained by the fixed local overpass times of sun-synchronous orbit satellites, spaceborne CALIOP data cannot be used to investigate the cloud diurnal cycles. Furthermore, due to the large receiver FOV of the CALIOP lidar telescope, strong multiple scattering effects occur when detecting liquid water clouds. Consequently, the liquid cloud depolarization ratios observed by CALIOP do not approach 0 like those from ground-based lidars, but instead exhibit characteristics of high backscatter and high depolarization. In contrast, the ground-based dual-angle lidar configuration employed in this study not only captures HOIC signals with extremely low depolarization ratios approaching 0, but also finely characterizes their full diurnal evolution.

While Figure 8 presents the distribution of mean values, the median distributions were also calculated during data processing. The two distributions exhibit consistent features with similar conclusions and are therefore not shown.

Figure 9 illustrates the daily evolution of the abundance of HOICs obtained using the relaxed cloud mask scheme. The cloud abundance here is defined as the ratio of the number of identified HOIC data points to the total number of valid lidar detections within a specific time-temperature grid cell. The temporal and temperature resolutions for the gridding process are set to 30 min and 2 K, respectively. The red dashed lines in the figure indicate the typical formation temperature regime for plate-like ice crystals (−22 °C to −8 °C). It can be observed that most of the HOIC data points are concentrated within this interval, whereas they seldom appear in environments colder than −40 °C.

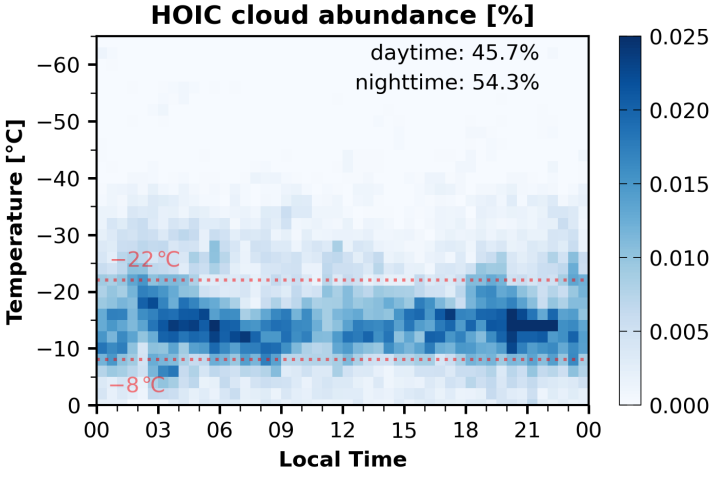

Figure 9. Local time–temperature cross-sections displaying the cloud abundance of HOICs based on a relaxed cloud mask. The data are gridded with a 30-min temporal resolution and a 2-K temperature resolution. The daytime and nighttime proportions of HOIC are noted in the upper-right part. The upper and lower limits of the typical formation temperature regime for plate-like ice crystals (−22 °C and −8 °C) are also indicated with red dashed lines.

https://doi.org/10.5194/egusphere-2026-3314
Preprint. Discussion started: 16 June 2026

The diurnal evolution of HOIC exhibits some variations, with larger occurrences in the periods: 02:00–09:00 and 16:00–22:00. To quantitatively evaluate the diurnal discrepancy, this study utilized the Python Astral library (Kennedy, 2023) to precisely calculate the daily sunrise and sunset times in Beijing, thereby strictly categorizing the HOIC data into daytime and nighttime. Statistical results indicate a slightly higher occurrence proportion of HOIC at night (54.3%) compared to the daytime (45.7%), further corroborating its characteristic of weak diurnal variability.

4.4 Environmental relationships and links to SWCs

Next, this study further investigates the dependence of HOICs and ROICs on macroscopic environmental variables, such as horizontal wind speed and temperature. The analytical approach in this section is similar to that described in Sect. 4.2 of Wu et al. (2025), but it utilizes observational data from the entire year of 2022. By significantly expanding the sample size to over 300,000 HOIC data points and over 1.4 million ROIC data points, the statistical results in this section are more representative and statistically significant in terms of climatological characteristics.

From a dynamical perspective, Figure 10a reveals a significant difference in the horizontal wind speed distributions between HOIC and ROIC. Compared to ROIC, HOIC tends to form in environments with lower horizontal wind speeds, with most of the HOIC samples exhibiting wind speeds below 40 m s^{-1}. Conversely, the wind speed distribution for ROIC is much broader, with a substantial presence even in high wind speed regions exceeding 40 m s^{-1}. From an aerodynamic standpoint, higher horizontal wind speeds are typically accompanied by stronger environmental wind shear and atmospheric turbulence. These perturbations disrupt the stable aerodynamic falling posture of ice crystals, causing them to tumble and thus exhibit random orientations. In contrast, a weaker wind field provides a stable dynamical background for ice crystals to maintain a horizontal orientation. This observation also corroborates the results of Garrett et al. (2025), which concluded that the mean horizontal wind field plays a key role in modulating the spatial orientation and fall velocity of hydrometeor particles.

From a thermodynamic perspective, Figure 10b shows that the two types of ice crystals are distinctly separated in temperature space. The ambient temperatures where HOICs exist are significantly higher than those for ROICs, exhibiting an extremely sharp distribution peak between −22 °C and −8 °C. Specifically, the median and mean temperatures of HOIC occurrences are −13.8 °C and −14.0 °C, respectively. This temperature regime is of critical significance in cloud microphysics: according to classical ice crystal growth theory, −22 °C to −8 °C is precisely the core temperature zone for the growth of plate and dendrite ice crystals. During their descent, aerodynamic drag tends to stabilize these flat ice crystals with their broad faces nearly normal to the direction of motion, thereby resulting in horizontal alignment. In contrast, the overall temperature distribution of ROIC is significantly lower (median −36.8 °C, mean −34.7 °C). Ice crystals generated in such cold environments are predominantly columnar or irregular polyhedra; furthermore, they are more susceptible to aggregation, making them much more likely to exhibit random orientations.

https://doi.org/10.5194/egusphere-2026-3314
Preprint. Discussion started: 16 June 2026

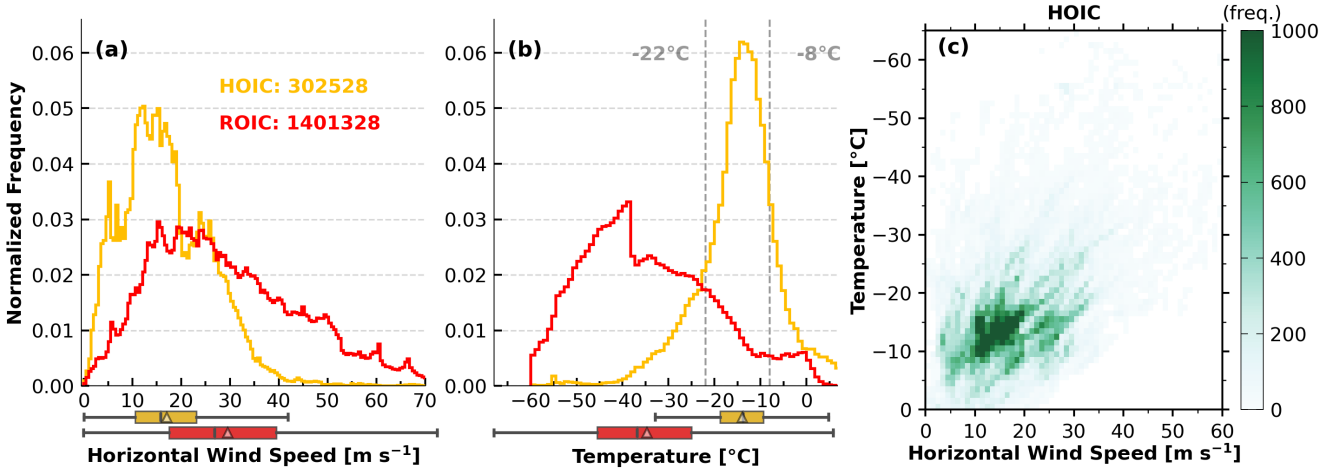

Figure 10. Environmental-variable distributions for the various cloud-phase classes during 2022. (a) The normalized histogram of horizontal wind speed for HOICs (orange) and ROICs (red), with boxplots shown below the x-axis. Boxes span the lower to upper quartiles; gray lines mark medians and triangles mark means. The whiskers reach either the data extremes or 1.5 times the interquartile range. (b) The normalized histogram of temperature for HOICs and ROICs, with boxplots shown below the x-axis. (c) Joint density of horizontal wind speed and ambient temperature for HOIC, with darker green marking more frequent HOIC observations.

Figure 10c further presents the joint density distribution of HOIC in the two-dimensional space of horizontal wind speed and temperature. The high-frequency concentration region of HOIC (the dark green core) is clearly confined within an envelope characterized by relatively high temperatures (−5 °C to −25 °C) and low wind speeds (3 to 30 m s^{-1}). Notably, within the dense regions of HOIC occurrence, environment temperature and horizontal wind speed show a distinct negative correlation (i.e., lower temperatures correspond to higher wind speeds). This not only conforms to the general meteorological rule of the mid-to-upper troposphere—where temperature decreases and wind speed increases with altitude—but also clearly delineates the "composite temperature-wind threshold boundary" required to maintain the horizontal alignment of ice crystals.

The temperature range where HOICs occur largely coincides with that in which SWCs are typically observed. To characterize the spatial association between HOICs and SWC, we consider the Euclidean distance from each ice-crystal-phase data point to the nearest overlying SWCs, as defined in Sect. 4.5 of our previous study (Wu et al., 2025): the root-sum-square of its horizontal and vertical offsets from that SWC. Here the vertical offset is the height gap between the two bins, whereas the horizontal offset equals the ERA5 horizontal wind multiplied by their time gap. This distance provides a quantitative measure of the proximity between HOICs and SWCs. The following presents the statistical results for the full year of 2022. The requirement to find the corresponding overlying SWC is that it precedes the ice crystals temporally and is located spatially above them, ice-crystal bins without such an overlying SWC are excluded. This requirement is consistent with the physical mechanism of ice crystal sedimentation. After this filtering, more than 200,000 valid HOIC and ROIC data points satisfied these criteria.

Figure 11 visually compares the Euclidean distance distributions from HOICs and ROICs to the overlying SWCs. The median distance from HOICs to SWCs is only 12.7 km, whereas the median for ROICs reaches 58.3 km, with mean distances

https://doi.org/10.5194/egusphere-2026-3314
Preprint. Discussion started: 16 June 2026

exhibiting a similarly pronounced contrast (83.0 km vs. 176.5 km). To rigorously verify this distinction, two-sample Kolmogorov-Smirnov and Mann-Whitney U tests were performed, both confirming a statistically significant difference ($p \ll 0.001$). Furthermore, Cliff's delta (d) was calculated to quantify the effect size without relying solely on p-value significance. The resulting value of $d = -0.32$ indicates a substantial systematic shift approaching a medium effect size (Romano et al., 2006). Together, these quantitative results provide strong evidence that HOICs typically exist in much closer physical proximity to SWCs than ROICs.

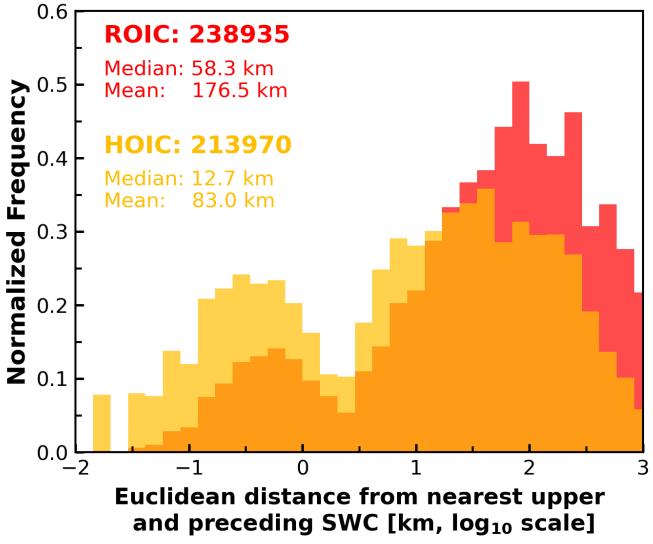

Figure 11. The normalized frequency of the Euclidean distances between HOICs, ROICs, and overlying SWCs. This normalized histogram utilizes data from the entire year of 2022, with the x-axis on a $\log_{10}$ scale in kilometers (km). The orange and red shading give the HOIC and ROIC distributions, with their median and mean distances annotated in the top-left part. Note: To ensure a causal relationship, the selected SWCs must temporally precede and be located spatially above the observed ice crystals.

This phenomenon is underpinned by a distinct cloud microphysical mechanism. Building on the case analyses of different cloud-top temperatures presented in Sect. 3.2, we propose that the formation of HOICs is closely linked to microphysical processes dominated by supercooled liquid water layers, particularly Wegener–Bergeron–Findeisen growth. Ice crystals existing within or immediately below SWCs are typically pristine ice crystals newly formed (Radenz et al., 2021; Zhang et al., 2026b). Growing in a water-vapour-rich environment, these ice crystals often develop intact, large planar geometries (e.g., plate or dendritic shapes, Bailey and Hallett, 2009). Their small aspect ratios make them highly susceptible to aerodynamic drag during the initial stage of descent, enabling them to form and maintain a horizontal orientation.

As the ice crystals continue to fall, their Euclidean distance from the overlying SWC continuously increases. During this prolonged descent and evolution, the probability of ice crystals undergoing aggregation or riming increases significantly. These processes destroy the original flat and regular structure of the ice crystals and increase their asymmetry, which destabilizes their aerodynamic posture and ultimately causes them to transition from a horizontal to a random orientation.

https://doi.org/10.5194/egusphere-2026-3314
Preprint. Discussion started: 16 June 2026

Furthermore, SWCs typically exist in stable atmospheric stratification (Pruppacher and Klett, 2010). SWCs are in a highly sensitive metastable state, and unstable airflows can easily trigger their freezing (Yang et al., 2018). Conversely, HOICs also require a relatively stable stratification to be maintained (Garrett et al., 2015). This shared requirement for stability may be another reason why the Euclidean distance between HOICs and SWCs is short.

Moreover, the statistical results of this study provide additional observational support for previous research. Ross et al. (2017) reported a close relationship between HOICs and surface precipitation in midlatitude marine low clouds using CALIPSO and CloudSat satellite products, while previous studies (French et al., 2018; Silber et al., 2021) identified SWCs as key components of cold-cloud precipitation processes. The quantitative statistics of Euclidean distance in this study establish a direct spatial link between SWCs and HOICs, thereby supporting an observationally consistent link between HOIC occurrence and SWC-related precipitation.

It is worth emphasizing that, constrained by observational methods, Ross et al. (2017) noted that polar-orbiting satellites, including the Moderate Resolution Imaging Spectroradiometer (MODIS), CALIPSO, and CloudSat, cannot provide a sufficient temporal sampling rate to investigate the continuous dynamical processes underlying the phenomena related to HOIC and precipitation. Spaceborne active remote sensing platforms move extremely fast, typically acquiring only "snapshot" profiles of a certain region. Passive satellite sensors have limited penetration capabilities, making it difficult to resolve the vertical cloud-phase structure. In contrast, the dual-angle ground-based polarization lidar configuration employed in this study boasts the advantages of high temporal continuity and vertical resolution. Through continuous fixed-point observations from an Eulerian perspective, this study achieves high-resolution discrimination of supercooled water layers and ice crystals with different orientations, and precisely captures their relative positions and spatiotemporal evolution. These capabilities provide valuable insight for the investigation of cloud and precipitation microphysical mechanisms.

4.5 EDR and cloud radar observations of HOICs and ROICs

In the previous section we found a link between ice orientation and horizontal wind, within this section, we further examine how turbulence is associated with HOIC occurrence on the analysis of EDR that was retrieved from the zenith-pointing Doppler cloud radar. To avoid contamination from melting ice particles, this section only includes HOIC samples colder than −2.5 °C, following the temperature criterion used by Westbrook et al. (2010). Figure 12 illustrates the frequency distributions (Fig. 12a) and two-dimensional temperature dependencies (Figs. 12b, c) of the EDR in environments containing differently oriented ice crystals, based on the relaxed cloud mask scheme. Overall, as the ambient temperature increases (approaching 0 °C), the EDR within the ice-containing cloud layers exhibits a gradual upward trend for both HOIC and ROIC (Figs. 12b, c).

Under conditions of low EDR (i.e., relatively stable and laminar atmospheric environments), both HOICs and ROICs can exist extensively. However, as the EDR increases to 10^{-2} m^2 s^{-3} (i.e., >−2 on a log10 scale), the occurrence frequency of HOIC begins to decrease sharply (Fig. 12a). From an aerodynamic perspective, a high EDR implies the presence of intense microscale turbulent eddies and wind shear within the cloud. When the overturning torque generated by these fluid

https://doi.org/10.5194/egusphere-2026-3314
Preprint. Discussion started: 16 June 2026

perturbations exceeds the aerodynamic restoring torque of the ice crystal, the crystal's stable falling posture is disrupted. This causes the crystal to tumble and transition to a random orientation.

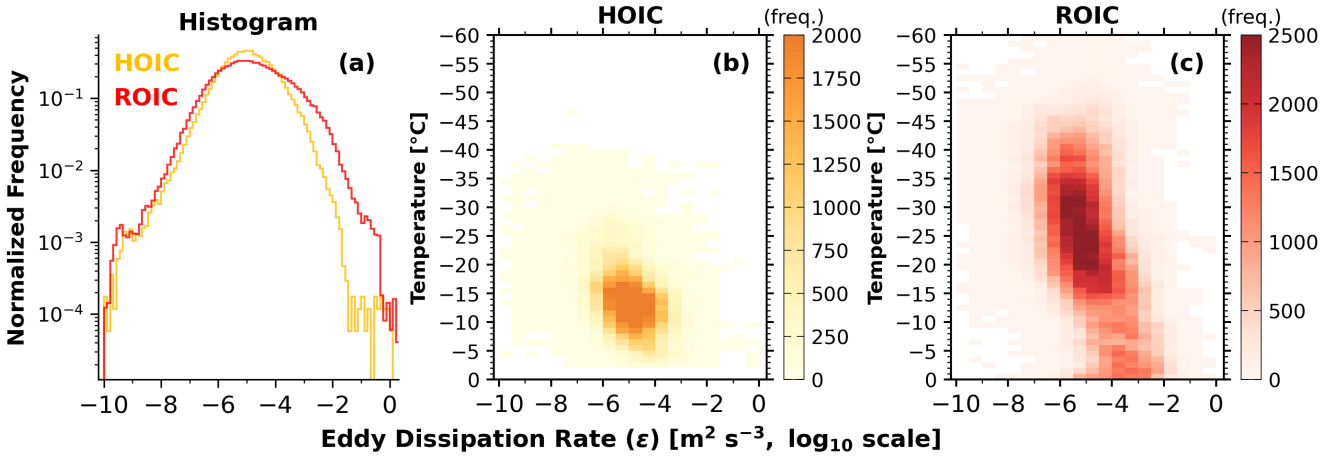

Figure 12. Statistical distributions of turbulent eddy dissipation rates (EDR, ε) for different orientations of ice crystals, based on the relaxed cloud mask. (a) Normalized histograms of ambient EDR for HOICs (orange) and ROICs (red), plotted on a $\log_{10}$ scale. (b) Scatter density plot of EDR versus temperature for HOIC. (c) Scatter density plot of EDR versus temperature for ROIC.

An EDR of approximately 10^{-2} m^2 s^{-3} can be considered one of the dynamical thresholds for maintaining large-scale horizontal alignment of ice crystals. In Appendix C, statistical results based on the rigorous cloud mask scheme (Fig. C1) highlight this turbulence cutoff characteristic even more clearly.

A further comparison of the two-dimensional density scatter plots in Figs. 12b and 12c reveal that the EDRs in HOIC environments are significantly biased toward lower values. To quantitatively evaluate this, non-parametric tests (Mann-Whitney U and Kolmogorov-Smirnov) were applied, both confirming a statistically significant difference in their overall EDR distributions ($p \ll 0.001$). Interestingly, the calculated Cliff's Delta yields a small overall effect size ($d = -0.060$). This seemingly modest effect size reflects the aforementioned microphysical reality: under weak turbulence, both ice crystal types extensively coexist, resulting in heavily overlapping distributions. The true physical distinction driving the statistical difference lies in the high-turbulence right tail. While ROICs maintain a certain density of data points even in extremely turbulent environments (EDR > 10^{-2} m^2 s^{-3}), HOICs exhibit a dynamical cutoff and are almost entirely absent.

This identified contrast in HOIC occurrence at EDR > 10^{-2} m^2 s^{-3} is further demonstrated in Fig. 13, which comprehensively shows the statistical distribution characteristics of direct millimeter-wave cloud radar observations (Doppler velocity, spectral width, and reflectivity factor) as well as retrieved physical quantities (EDR) across different temperature intervals, which will be described as follows in detail.

The following reports on the radar-based parameters. Figure 13a compares the Doppler velocities of the falling ice crystals with different orientations. Overall, as the temperature increases (approaching 0 °C), ice particles gradually grow, and their fall velocities increase accordingly. Notably, across all temperature intervals, the Doppler velocities of HOICs are systematically lower than those of ROICs. This difference is particularly prominent in the −20 °C to −10 °C range, where

https://doi.org/10.5194/egusphere-2026-3314
Preprint. Discussion started: 16 June 2026

HOIC frequently occurs. In the −30 °C to −20 °C range, although there is some overlap, a clear difference in the medians persists.

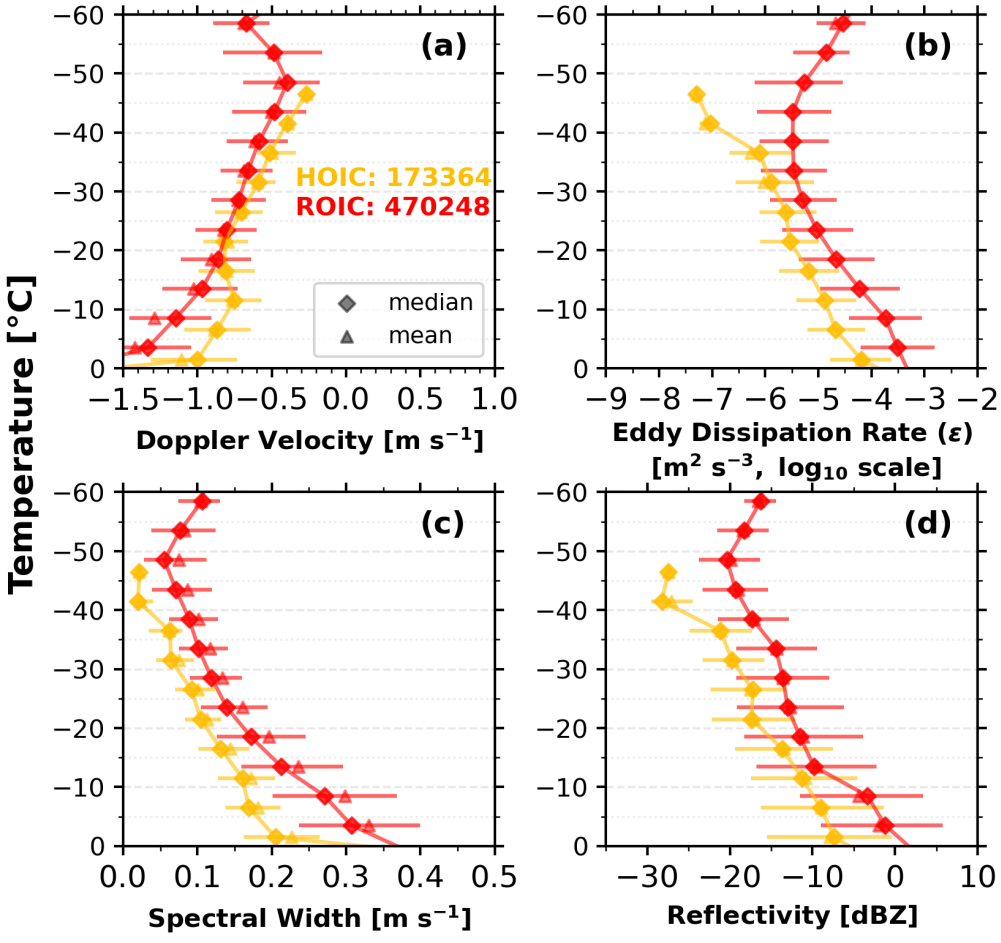

Figure 13. Distributions of cloud radar observations and retrievals across temperature intervals for different ice-crystal orientations: (a) Doppler velocity; (b) eddy dissipation rate; (c) Doppler spectral width; and (d) radar reflectivity factor. Diamonds and triangles denote the medians and means within each 5 °C temperature bin, respectively. The horizontal lines span the 25th–75th percentile range.

This phenomenon has a profound aerodynamic basis. As noted by Heymsfield and Iaquinta (2000), the horizontal orientation of an ice crystal causes its maximum cross-section to face the airflow, thereby significantly increasing the aerodynamic drag force and effectively slowing its terminal settling velocity. According to the fluid dynamic derivations by Pruppacher and Klett (2010), small ice crystals that have not undergone significant aggregation tend to maintain this quasi-horizontal stable posture, which maximizes drag, when the environmental Reynolds number is between 1 and 100. In contrast, ROICs often experience a sudden increase in mass due to aggregation or riming, or undergo tumbling caused by strong turbulent perturbations. This results in a reduction of their time-averaged drag coefficient, leading to larger terminal velocities under the influence of gravity.

https://doi.org/10.5194/egusphere-2026-3314
Preprint. Discussion started: 16 June 2026

Furthermore, the Doppler velocities observed here are slightly larger than those reported by Westbrook et al. (2010). For example, at −35 °C, they observed mean Doppler velocities of 0.25 and 0.3 $\mathrm{m\,s^{-1}}$ for HOIC and ROIC, while the corresponding values in this study are approximately 0.5 and 0.6 $\mathrm{m\,s^{-1}}$. This discrepancy likely reflects differences in observation instrument sensitivity: the backscattering cross-section of a millimeter-wave cloud radar scales with the sixth power of diameter (D^6). Consequently, the cloud radar volume scattering signal is naturally dominated by larger (and faster-falling) particles (Donovan and Van Lammeren, 2001; Bühl et al., 2015). Consistent with our estimates, He et al. (2021) observed 32 HOIC events in Wuhan using polarization lidar and estimated fall velocities of 0.28 to 1.0 $\mathrm{m\,s^{-1}}$ from depolarization ratio profiles, which is in good agreement with the findings in this study.

Figures 13b and 13c reveal the dependence of ice crystal orientation on atmospheric turbulence from the perspectives of both retrievals and direct observations. Figure 13b shows the variation in retrieved EDR for different ice crystal orientations across various temperature intervals. This figure can be considered an alternative representation of Figs. 12b and 12c. Figure 13 further quantifies the conclusions drawn from Figure 12: across all temperature intervals, the EDR in environments containing HOICs is significantly lower than that of ROICs, by nearly an order of magnitude on average. This is a novel finding with significant microphysical implications, providing valuable observational evidence for the parameterization of cloud microphysics schemes in numerical models, such as establishing turbulence cutoff thresholds for ice crystal orientation.

This conclusion is cross-validated by the Doppler spectral width distribution in Figure 13c. Doppler spectral width, corresponding to the second moment of the radar Doppler spectrum, is directly measured by cloud radar without additional retrieval. High spectral width directly reflects a large dispersion in the fall velocities of the particle population within the sampling volume, strong wind shear, beam broadening, and high atmospheric turbulence intensity (Shupe et al., 2012; Li et al., 2021). The statistical results show that HOICs are associated with lower spectral widths, indicating their existence in environments with weak turbulence. Only under such dynamically stable conditions can ice crystals steadily maintain a horizontal posture. Once ambient turbulence intensifies (characterized by increased spectral width and EDR), not only is the stable posture of the ice crystals disrupted (transitioning to ROIC), but the intense turbulent mixing may also increase the collision probability among particles (Chellini and Kneifel, 2024).

Figure 13d shows that the radar reflectivity factor (dBZ) for HOIC is systematically lower than that for ROIC across all temperatures. Because radar reflectivity is strongly weighted toward larger particles, approximately following a sixth-power dependence on the particle diameter (D^6) under the Rayleigh approximation, this further corroborates the inference of this study: HOICs represent relatively small, pristine ice crystals in stable environments that have not undergone significant aggregational growth. In contrast, ROICs contain abundant complex ice crystal aggregates with larger equivalent diameters resulting from aggregation, riming, or other intricate growth processes.

The single-profile case shown in Fig. 5 of Wu et al. (2025) reported that the reflectivity of ROIC at the cloud base was lower than that of the HOIC above it. This is likely not a contradiction, but rather a distinction between macro-statistics and micro-evolutionary stages. Actual observations indicate that the radar reflectivity factor of cloud radar is often smaller at cloud boundaries and larger in the middle of the cloud profile; cloud boundaries are typically on the verge of dissipation. In a single

https://doi.org/10.5194/egusphere-2026-3314
Preprint. Discussion started: 16 June 2026

cloud profile, the cloud base is usually located within the dissipation zone of the cloud boundary. After falling out of the cloud base, ice crystals undergo intense sublimation, leading to a sharp decrease in particle size and number concentration, which in turn causes a steep drop in radar reflectivity. In contrast, the statistics in this section—based on a large sample size from the entire year of 2022—cover HOIC and ROIC samples at various developmental stages within the cloud body. This filters out the interference from the edge dissipation effects of a single profile, thereby more accurately reflecting the microphysical size differences between the two orientation types of ice crystals throughout their entire life cycles.

Westbrook et al. (2010) pointed out that the distribution of cloud radar reflectivity factors in specular regions (HOIC) is almost identical to that in non-specular regions (ROIC). However, a closer inspection of their Fig. 19 reveals that HOICs may exhibit slightly lower dBZ values, particularly at temperatures below −20 °C.

4.6 Reynolds Number and particle diameter of HOICs

Wu et al. (2025) presented the retrieval results of the microphysical characteristics of HOICs based on a single case study on 13 October 2022. To obtain statistical laws with greater climatological representativeness, Fig. 14, in conjunction with Table 1, further illustrates the distributions of the lidar-cloud radar retrieved particle Reynolds number and model-equivalent diameter of HOICs during the entire year of 2022. This retrieval utilized the same aerodynamic model as in Wu et al. (2025), assuming HOICs as hexagonal plates, and the resulting values should therefore be interpreted as first-order estimates rather than exact particle properties. The statistical analysis comprises over 150,000 valid retrieval points, covering a diverse range of macro- and micro-environmental cloud characteristics, thereby ensuring statistical significance.

As shown in Fig. 14a and Table 1, the annual statistics for HOIC diameters are primarily concentrated from 700 to 2000 μm, with median and mean values 1187 μm and 1249 μm, respectively. Compared to the single case (Wu et al., 2025), the annual scale distribution is broader, which reasonably reflects the complex and diverse microphysical evolutionary stages of cloud bodies in nature. It should be specifically noted that the HOIC scales retrieved in this study are overall larger compared to typical ice crystal populations. This is primarily limited by the inherent detection mechanism of millimeter-wave cloud radar: under the Rayleigh scattering approximation, the particle backscattering cross-section scales with the sixth power of diameter (D^6) (Li, 2021). For the large HOIC particles retrieved here, however, this should be regarded as an approximate size-weighting argument rather than a strict Rayleigh-regime relationship. Consequently, the mean Doppler velocity observed by the cloud radar is actually a reflectivity-weighted fall velocity (Bühl et al., 2015), which is naturally dominated by the larger, faster-falling ice crystals within the cloud volume. In contrast, lidar backscattering is typically proportional only to the cross-sectional area (D^2) (Stephens, 1994; Bohren and Huffman, 1998; Donovan and Van Lammeren, 2001). While retrievals based on lidar Doppler velocities would theoretically be biased toward smaller ice crystals, this study utilizes cloud radar data, which are inherently more sensitive to the 'larger ice crystal population' that maintains a horizontal orientation. Consequently, the samples in this study likely miss small-scale HOICs. For instance, in Fig. B5 of Appendix B, the ground-based lidars identified HOIC in high-altitude cirrus (approximately 11 km), but the millimeter-wave cloud radar did not actually detect this cloud layer. Due to the lack of Doppler velocity observations, the scale retrieval for HOIC in that case could not be implemented. Since high-

https://doi.org/10.5194/egusphere-2026-3314
Preprint. Discussion started: 16 June 2026

altitude cirrus clouds form at extremely low temperatures with limited water vapor supply, they typically consist of smaller ice particles (Heymsfield et al., 2017; Krämer et al., 2020).

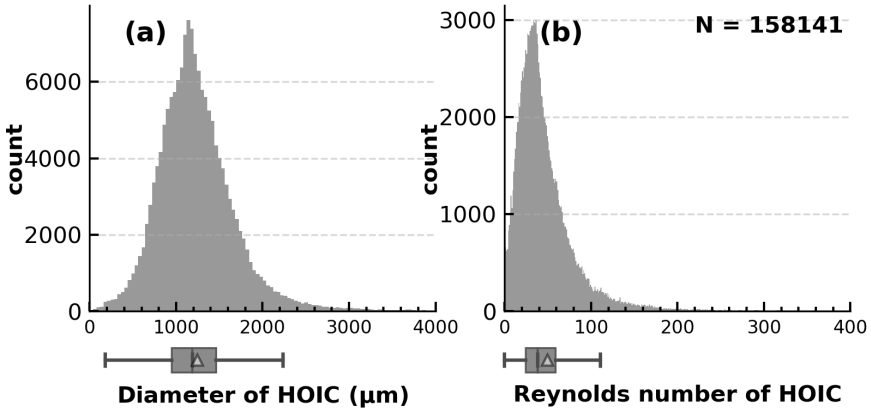

Figure 14. Statistical distributions of equivalent diameter and particle Reynolds number for HOICs during 2022, derived from an aerodynamic retrieval model. (a) Normalized frequency histogram of HOIC equivalent diameter. (b) Corresponding frequency histogram of particle Reynolds number. The boxplots beneath each horizontal axis span the first-to-third quartile range, with the internal vertical line and triangle representing the median and mean. This figure incorporates over 150,000 valid retrievals.

Figure 14b presents another critical fluid dynamic parameter governing ice crystal orientation: the Reynolds number (*Re*), which characterizes how the surrounding air responds to the motion of sedimenting ice crystals. The histogram reveals that HOICs (with a third quartile of 59) mostly have Reynolds numbers distributed between 0 and 100, with cases exceeding 200 being rare. This implies that *Re* must remain relatively small to maintain the stable horizontal alignment of ice crystals.

Here, *Re* quantifies the relative importance of inertial and viscous effects during the ice crystal's descent, directly determining the wake instability of the microscopic flow field around the crystal. From an aerodynamic perspective, at low *Re*, the fluid maintains a stable laminar state over the ice crystal surface, and the forces on the crystal are uniform, allowing it to stably maintain a horizontal orientation that maximizes drag. Once *Re* exceeds a critical threshold, boundary layer separation occurs behind the crystal, generating periodic vortex shedding. These asymmetric aerodynamic lift forces and torques induce pitching and fluttering motions, eventually disrupting the horizontal posture (Pruppacher and Klett, 2010).

These retrieval results are consistent with laboratory fluid dynamic experiments. For example, List and Schemenauer (1971) observed the fall of solid snowflake particle analogs in salt solutions and glycerin-water mixtures and found that for five types of planar ice crystal geometries, stable descent was maintained when $Re < 100$. When $Re \approx 200$, discs, broad-branched analogs and hexagonal plates began to exhibit small oscillations. Recently, sedimentation experiments by Stout et al. (2024) using 3D-printed plate analogs in a water-glycerin mixture further confirmed that solid hexagonal plates begin to undergo significant rocking and vibration when *Re* reaches 237.

https://doi.org/10.5194/egusphere-2026-3314
Preprint. Discussion started: 16 June 2026

Table 1. Summary statistics of the retrieved HOIC diameters and Reynolds numbers in 2022

Statistic	Diameter [μm]	Reynolds number
5th percentile	612	9
First quartile	950	24
Median	1187	38
Third quartile	1464	59
95th percentile	2036	118
Mean	1249	49

5 Summary and conclusions

This work provides a year-long ground-based statistical characterization of horizontally oriented ice crystals (HOICs) over Beijing, China. The dataset combines observations from a zenith-pointing micropulse lidar, a collocated 15° off-zenith AVORS polarization lidar, and a Ka-band cloud radar with supporting ERA5 reanalysis and radiosonde profiles. Building on a previously developed range-resolved classification framework (Wu et al., 2025), we combined case studies and annual statistics to investigate the occurrence characteristics, environmental conditions, and dynamical and microphysical properties of HOICs throughout 2022. First, we utilized a relaxed cloud mask scheme to correct for the potential missed HOIC range bins close to the lidar attenuation region. The HOIC classification results were subsequently verified by a collocated sun dog photograph on 14 December 2022, providing robust independent optical evidence.

Based on the reliable identification of HOICs, their macrophysical and microphysical characteristics, as well as the environmental triggering mechanisms were systematically analyzed. Annual statistical data indicate that the occurrence frequency of HOICs among ice-containing cloud data points in the Beijing area is approximately 15%, with a maximum of about 25% in summer, indicating that they represent a non-negligible component of natural ice-containing clouds. The HOIC diurnal variability is comparatively weak, with a slightly higher proportion at night than during daytime. Macroscopically, HOICs tend to occur in stable atmospheric stratifications at temperatures of −22 °C to −8 °C and relatively weak horizontal wind speeds (0–40 m s^{-1}). The typical duration of HOIC events is 0.3–2 hours, with a horizontal distribution scale of 10–100 km, representing typical mesoscale weather characteristics. Regarding microphysical and dynamical characteristics, retrieval results based on an aerodynamic model and cloud radar Doppler velocities show that the equivalent diameters of HOICs are mainly concentrated between 700 and 2000 μm (median: 1187 μm, mean: 1249 μm). The corresponding Reynolds numbers (*Re*) are mostly less than 100 (median: 38, third quartile: 59), and their fall Doppler velocities are systematically lower than those of randomly oriented ice crystals (ROICs).

Crucially, our observations further reveal that overlying supercooled liquid water clouds (SWCs) and low turbulence play key roles in maintaining the horizontal orientation of ice crystals. Observations confirm that the Euclidean distance from

https://doi.org/10.5194/egusphere-2026-3314
Preprint. Discussion started: 16 June 2026

HOICs to the overlying SWCs (median: 12.7 km) is significantly shorter than that for ROICs (median: 58.3 km). This finding quantitatively supports the important role of SWCs in the formation process of HOICs: pristine ice crystals with intact and large basal planes generated within the SWC layer, compared to aged and irregularly shaped ice crystals, are more likely to form and maintain horizontal orientation under the influence of aerodynamic drag during their fall. Cases with varying SWC top temperatures, as well as the presence of supercooled liquid water at the tops of multiple HOIC layers, also support this conclusion. Meanwhile, turbulence is a key dynamical factor that disrupts the horizontal orientation of ice crystals. Statistical analyses in this study indicate that HOICs exist in environments where the turbulent eddy dissipation rate (EDR) is less than 10^{-2} m^2 s^{-3}. When the EDR exceeds this critical threshold, the occurrence frequency of HOICs decreases sharply. Within the same temperature range, HOICs exhibit average EDR values almost one order of magnitude smaller than those associated with ROICs.

Nevertheless, several limitations should be acknowledged. Like all lidar-based cloud research, the laser light attenuation problem is unavoidable. Future hydrometeor orientation identification using cloud radar could be employed to compensate for this defect (Hajipour, 2025). Furthermore, the present analysis is based on observations from a single site and a single year, and some statistical results depend on the adopted cloud-masking and retrieval assumptions. In particular, the relaxed cloud mask improves cloud-top coverage but may still introduce some classification uncertainties, and the diameter and Reynolds number retrievals are conditioned on an idealized aerodynamic representation of HOICs. In the future, it would be desirable if such data sets are available at different sites over several years to also further examine the sensitivity of the inferred HOIC properties to cloud classification strategy, ice-crystal habit assumptions, and environmental variability.

https://doi.org/10.5194/egusphere-2026-3314
Preprint. Discussion started: 16 June 2026

Appendix A: Conceptual diagram of a sun dog

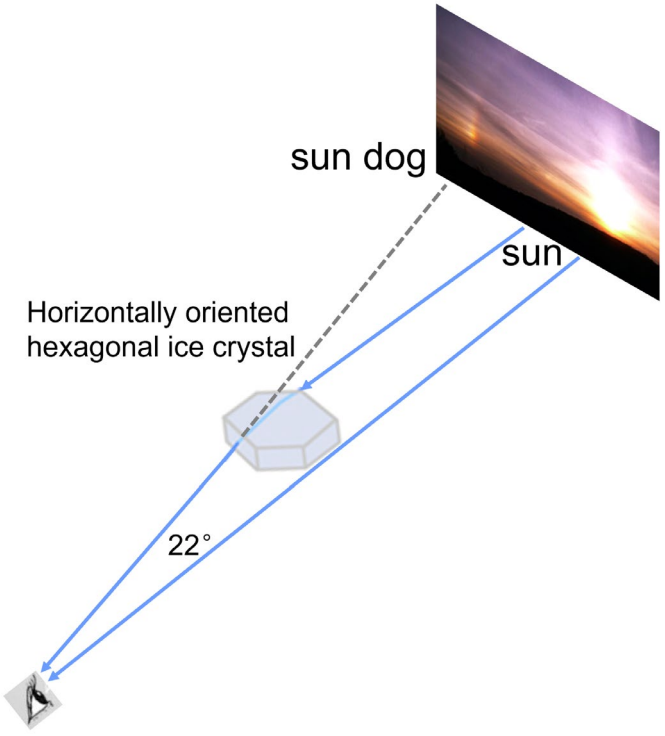

Figure A1. Schematic diagram illustrating the formation mechanism of sun dog. The solid blue line represents the parallel sunlights emitted by the sun, and the gray dashed line indicates the backward extension of the sunlight rays as seen by the observer. Sunlight undergoes two refractions within the prism facets of horizontally oriented hexagonal ice crystals, resulting in a 22° deviation in the light propagation path. The observer perceives a light spot at the intersection of the backward extensions of multiple light rays; this light spot is a virtual image, which is known as a sun dog (parhelion).

Appendix B: Direct observed quantities in the Sect. 3 case studies

Figures B1 to B5 below show the direct observed quantities corresponding to the cases presented in the Sect. 3.2, for scenarios when cloud-top temperatures are about −15 °C to −55 °C.

https://doi.org/10.5194/egusphere-2026-3314
Preprint. Discussion started: 16 June 2026

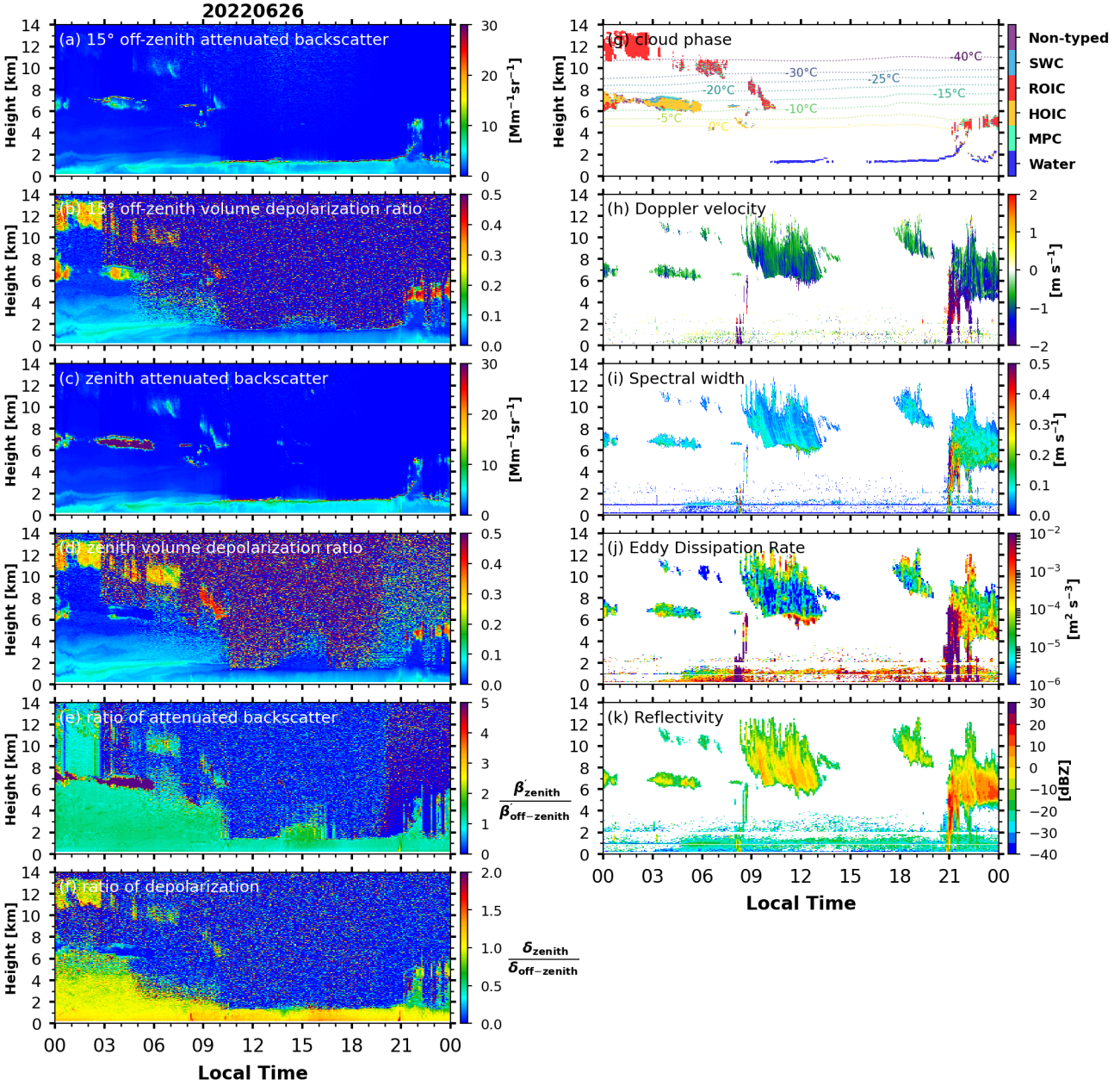

Figure B1. Observations on 26 June 2022 from lidar (a–g) and zenith-pointing Ka-band cloud radar (h–k) , shown as time–height cross sections (5 min / 15 m resolution for a–g, 13 s / 30 m for h and i, chosen to capture the Doppler-velocity variation, 5 min / 30 m for j and k). (a) attenuated backscatter from the 15° off-zenith pointing lidar. (b) volume depolarization ratio from the 15° off-zenith-pointing lidar. (c) attenuated backscatter from the zenith-pointing lidar. (d) volume depolarization ratio from the zenith-pointing lidar. (e) The ratio of attenuated backscatter between zenith-pointing and off-zenith-pointing lidar. (f) The ratio of volume depolarization between zenith-pointing and off-zenith-pointing lidar. (g) Cloud-phase categorization with the ERA5 isotherm overlaid. Here SWC, ROIC, HOIC, and MPC denote supercooled liquid water cloud, randomly oriented ice crystal, horizontally oriented ice crystal, and mixed-phase cloud. (h, i, k) Momentum quantities detected by the cloud radar: Doppler velocity, spectral width and reflectivity. (j) The eddy dissipation rate (EDR, ϵ) retrieved by cloud radar. The cloud-top temperature of the layer hosting the horizontally oriented ice crystals is approximately −15 °C, corresponding to the plate and dendritic crystal growth regime.

https://doi.org/10.5194/egusphere-2026-3314
Preprint. Discussion started: 16 June 2026

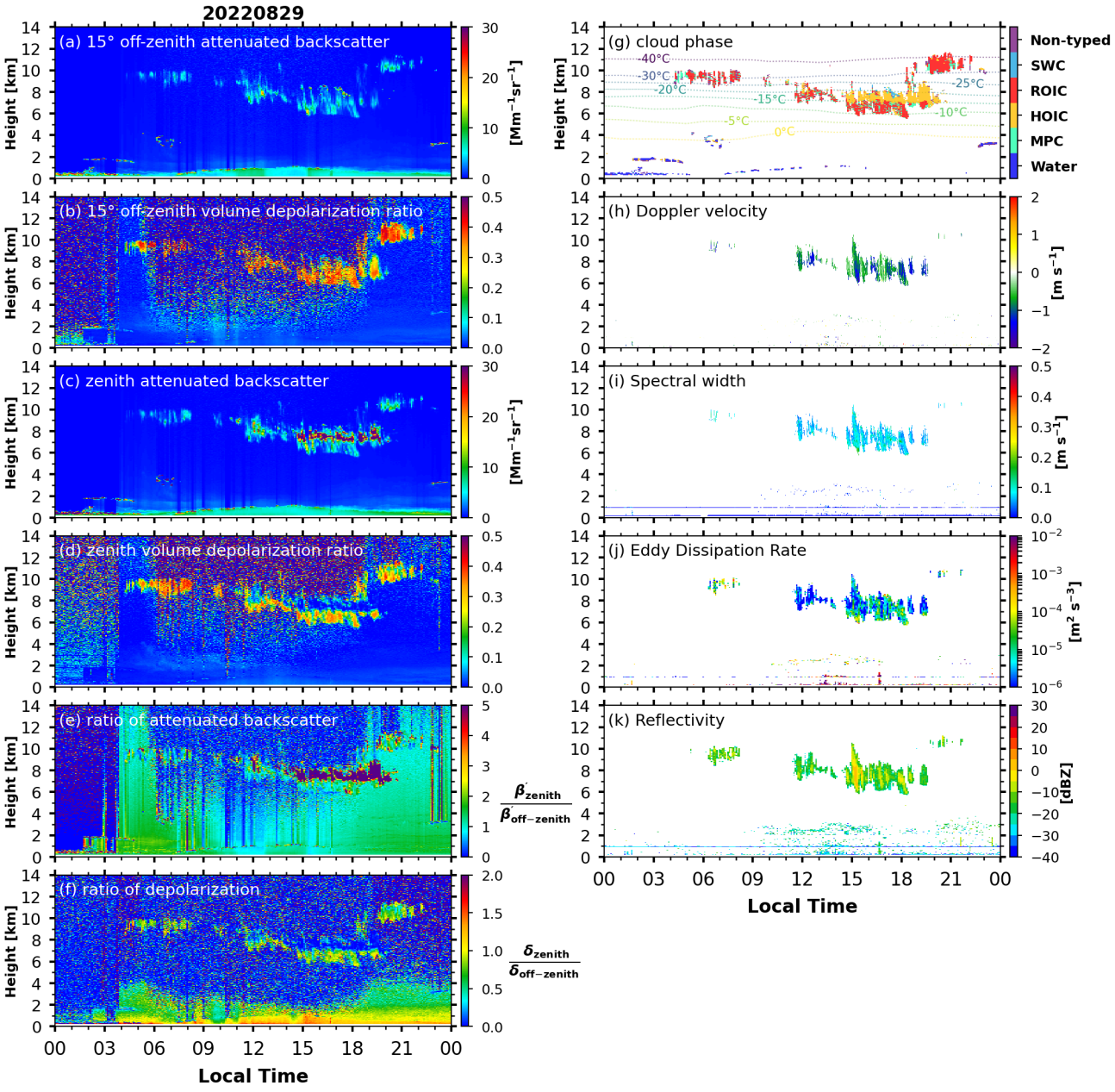

Figure B2. As in Fig. B1, but showing lidar and radar observations on 29 August 2022. The HOIC-containing layer has cloud-top temperature from −25 to −20 °C, corresponding to the plate-like crystal growth regime.

https://doi.org/10.5194/egusphere-2026-3314
Preprint. Discussion started: 16 June 2026

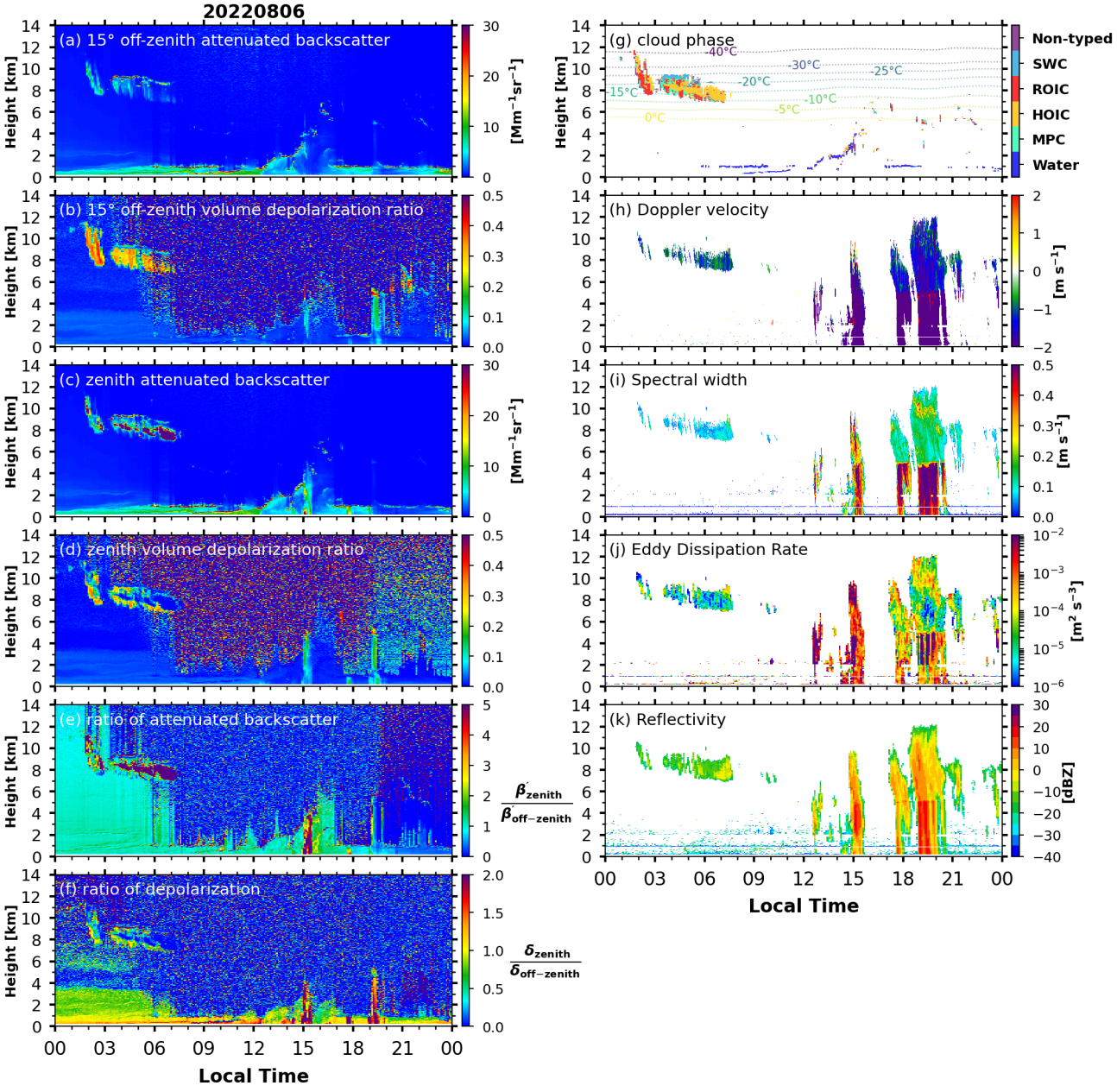

Figure B3. As in Fig. B1, but showing lidar and radar observations on 6 August 2022. The HOIC-containing layer has cloud-top temperature of approximately −30 to −25 °C, corresponding to the plate-based polycrystal growth regime.

https://doi.org/10.5194/egusphere-2026-3314
Preprint. Discussion started: 16 June 2026

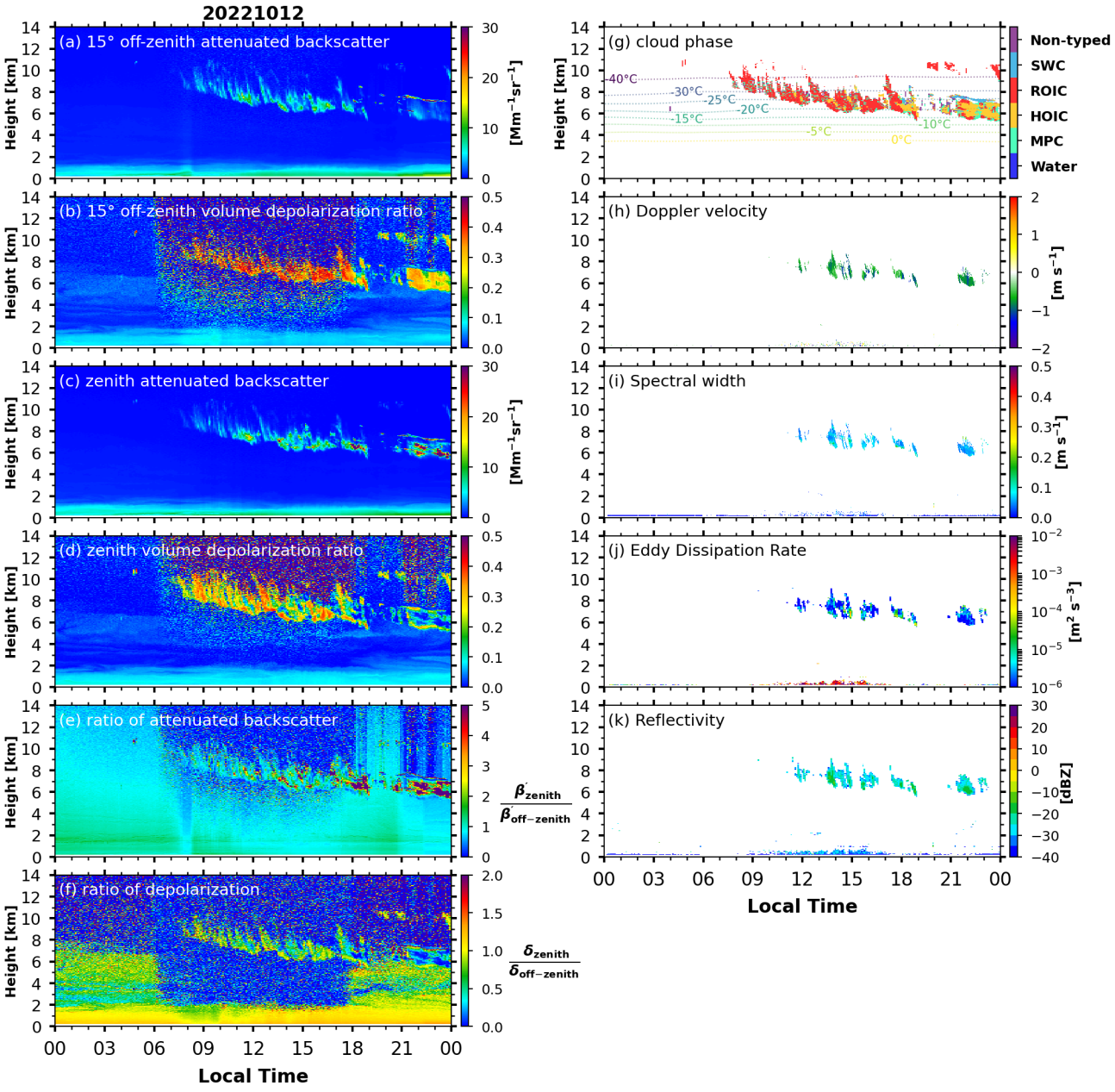

Figure B4. As in Fig. B1, but showing lidar and radar observations on 12 October 2022. The HOIC-containing layer has cloud-top temperature from −40 to −25 °C.

https://doi.org/10.5194/egusphere-2026-3314
Preprint. Discussion started: 16 June 2026

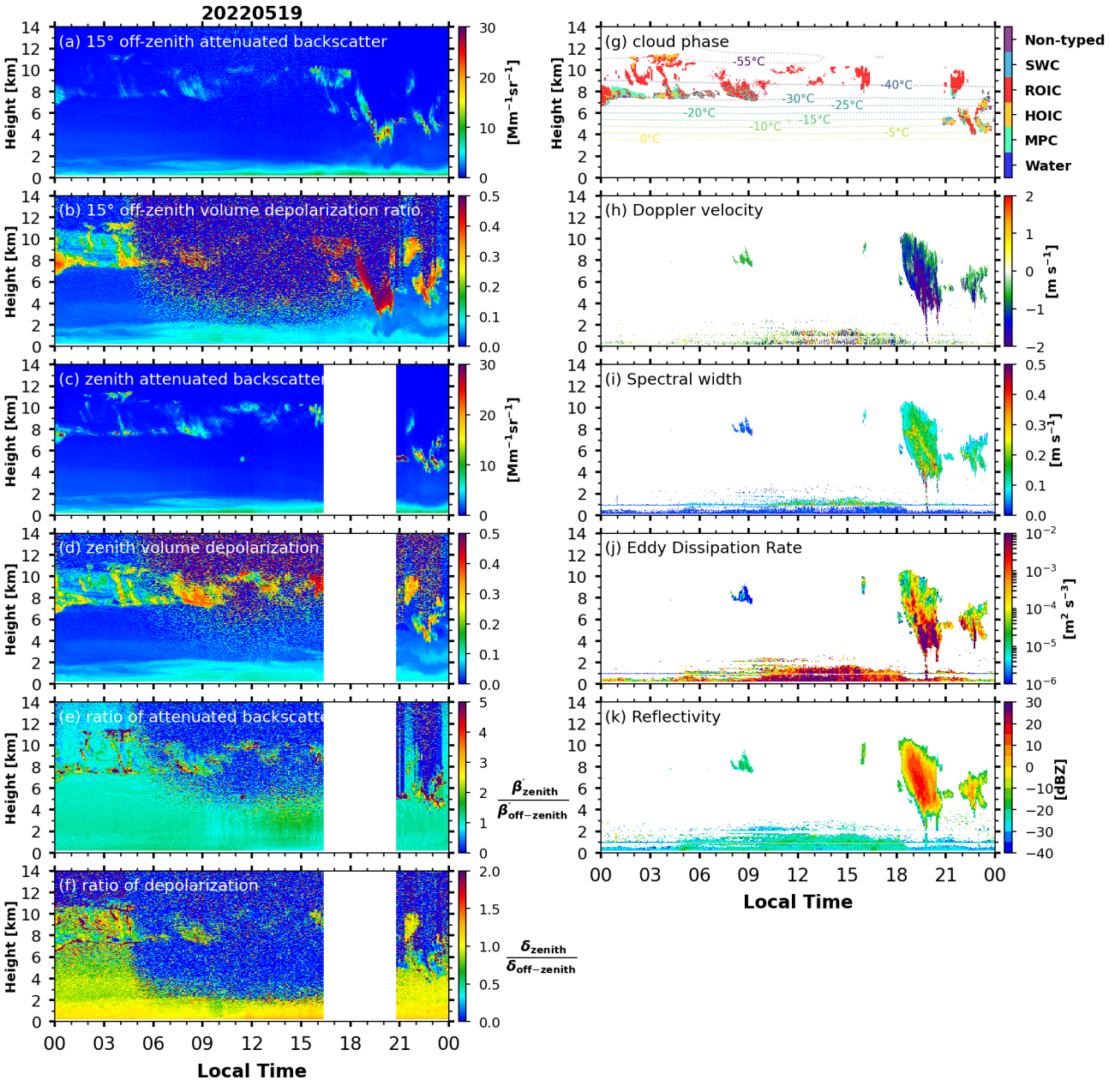

Figure B5. As in Fig. B1, but showing lidar and radar observations on 19 May 2022. The HOIC-containing layer has a cloud-top temperature around −55 °C.

https://doi.org/10.5194/egusphere-2026-3314
Preprint. Discussion started: 16 June 2026

Appendix C: Supplementary statistical figures

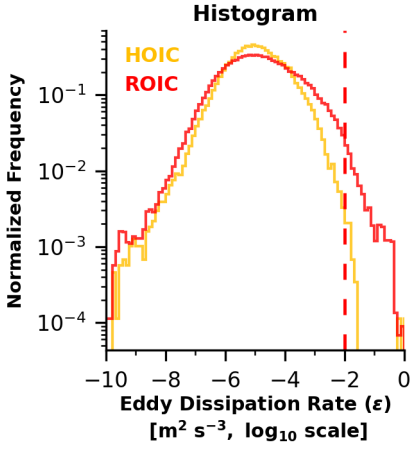

Figure C1. Normalized frequency histograms of ice crystals with different orientations at different turbulent dissipation rates, using the rigorous cloud identification scheme. The vertical red dashed line represents the turbulent dissipation rate threshold of 10^{-2} m^2 s^{-3} identified in this study, at which the occurrence frequency of HOICs decreases rapidly.

Appendix D: Abbreviations and symbols

AD-Net	Asian Dust and Aerosol Lidar Observation Network
CALIOP	Cloud-Aerosol Lidar with Orthogonal Polarization
CALIPSO	Cloud-Aerosol Lidar and Infrared Pathfinder Satellite Observations
CARLNET	China Aerosol Raman Lidar Network
CTT	cloud-top temperature
DFS	depth-first search
DJF	December–January–February
ECMWF	European Centre for Medium-Range Weather Forecasts
EDR(ε)	eddy dissipation rate
ERA5	ECMWF Reanalysis v5
FOV	field of view
HOIC	horizontally oriented ice crystal
JJA	June–July–August
MAM	March–April–May
MPC	mixed-phase cloud

https://doi.org/10.5194/egusphere-2026-3314
Preprint. Discussion started: 16 June 2026

MPL	Micro Pulse Lidar
MPLNET	Micro-Pulse Lidar Network
RH	relative humidity
ROIC	randomly oriented ice crystal
SNR	signal-to-noise ratio
SON	September–October–November
SWC	supercooled liquid water cloud
WMO	World Meteorological Organization
d	Cliff's Delta
Re	Reynolds number
β'	attenuated backscatter
β'_{zenith}	zenith-pointing lidar attenuated backscatter
$\beta'_{\mathrm{off-zenith}}$	off-zenith-pointing lidar attenuated backscatter
$\delta_{\mathrm{v}}(\delta)$	volume depolarization ratio
δ_{zenith}	zenith-pointing lidar volume depolarization ratio
$\delta_{\mathrm{off-zenith}}$	off-zenith-pointing lidar volume depolarization ratio

Data availability

Radiosonde data are available at http://weather.uwyo.edu/upperair/sounding.html (Beijing Radiosonde, 2022). The ERA5 data can be obtained at https://cds.climate.copernicus.eu/. The Python astral library used for solar time calculations is openly available at https://github.com/sffjunkie/astral. The lidar and radar data used in this study can be obtained from the authors upon reasonable request by contacting cfzhao@pku.edu.cn.

Author contributions

ZW and CL designed the study. ZW carried out the measurements, characterized the instruments, and performed the data analysis. PS, AA, HB, CJ, YH, JL and CZ contributed to the scientific interpretation and the conceptualization of the work. ZW, CJ and YH developed the classification scheme. ZW wrote the manuscript with guidance from PS, HB, CJ, JL and CZ. HB and CJ supported the depolarization calibration. CL and CZ obtained the research funding. All co-authors reviewed and edited the manuscript.

https://doi.org/10.5194/egusphere-2026-3314
Preprint. Discussion started: 16 June 2026

Competing interests

The authors declare that they have no conflict of interest.

Disclaimer

Copernicus Publications remains neutral with regard to jurisdictional claims in published maps and institutional affiliations.

Acknowledgements

The authors thank ECMWF for providing ERA5 reanalysis data, AVORS Technology for lidar data, and the University of Wyoming for access to Beijing radiosonde data. The authors thank Haoran Li for insightful discussions on cloud radar observations and cloud physics. We also thank the colleagues who supported operation of the lidar-radar system at our observation site.

Financial support

This study was partly funded by the National Natural Science Foundation of China (grant no. 42230601). Zhaolong Wu appreciates the support from the China Scholarship Council to conduct this research under the grant no. 202306010350.

References

Auguste, F., Magnaudet, J., and Fabre, D.: Falling styles of disks, J. Fluid Mech., 719, 388–405, https://doi.org/10.1017/jfm.2012.602, 2013.

Bailey, M. P. and Hallett, J.: A comprehensive habit diagram for atmospheric ice crystals: Confirmation from the laboratory, AIRS II, and other field studies, Journal of the Atmospheric Sciences, 66, 2888–2899, https://doi.org/10.1175/2009JAS2883.1, 2009.

Bohren, C. F. and Huffman, D. R.: Absorption and Scattering of Light by Small Particles, 1st ed., Wiley, https://doi.org/10.1002/9783527618156, 1998.

Bréon, F.-M. and Dubrulle, B.: Horizontally oriented plates in clouds, Journal of the Atmospheric Sciences, 61, 2888–2898, https://doi.org/10.1175/JAS-3309.1, 2004.

Bühl, J., Leinweber, R., Görsdorf, U., Radenz, M., Ansmann, A., and Lehmann, V.: Combined vertical-velocity observations with Doppler lidar, cloud radar and wind profiler, Atmos. Meas. Tech., 8, 3527–3536, https://doi.org/10.5194/amt-8-3527-2015, 2015.

https://doi.org/10.5194/egusphere-2026-3314
Preprint. Discussion started: 16 June 2026

Chellini, G. and Kneifel, S.: Turbulence as a Key Driver of Ice Aggregation and Riming in Arctic Low-Level Mixed-Phase Clouds, Revealed by Long-Term Cloud Radar Observations, Geophysical Research Letters, 51, e2023GL106599, https://doi.org/10.1029/2023GL106599, 2024.

Chepfer, H., Brogniez, G., Goloub, P., Bréon, F. M., and Flamant, P. H.: Observations of horizontally oriented ice crystals in cirrus clouds with POLDER-1/ADEOS-1, Journal of Quantitative Spectroscopy and Radiative Transfer, 63, 521–543, https://doi.org/10.1016/S0022-4073(99)00036-9, 1999.

Chi, Y., Zhao, C., Yang, Y., Ma, Z., and Yang, J.: Cloud macrophysical characteristics in China mainland and east coast from 2006 to 2017 using satellite active remote sensing observations, Intl Journal of Climatology, 42, 8984–9002, https://doi.org/10.1002/joc.7790, 2022.

Cliff, N.: Dominance statistics: Ordinal analyses to answer ordinal questions, Psychological Bulletin, 114, 494–509, https://doi.org/10.1037/0033-2909.114.3.494, 1993.

Cormen, T. H., Leiserson, C. E., Rivest, R. L., and Stein, C.: Introduction to algorithms, Fourth edition., The MIT Press, Cambridge, Massachusett, 1291 pp., 2022.

Ding, H., Li, H., and Liu, L.: Improved spectral processing for a multi-mode pulse compression Ka–Ku-band cloud radar system, Atmospheric Measurement Techniques, 15, 6181–6200, 2022.

Donovan, D. P. and Van Lammeren, A. C. A. P.: Cloud effective particle size and water content profile retrievals using combined lidar and radar observations: 1. Theory and examples, J. Geophys. Res., 106, 27425–27448, https://doi.org/10.1029/2001JD900243, 2001.

French, J. R., Friedrich, K., Tessendorf, S. A., Rauber, R. M., Geerts, B., Rasmussen, R. M., Xue, L., Kunkel, M. L., and Blestrud, D. R.: Precipitation formation from orographic cloud seeding, Proc. Natl. Acad. Sci. U.S.A., 115, 1168–1173, https://doi.org/10.1073/pnas.1716995115, 2018.

Garrett, T. J., Yuter, S. E., Fallgatter, C., Shkurko, K., Rhodes, S. R., and Endries, J. L.: Orientations and aspect ratios of falling snow, Geophysical Research Letters, 42, 4617–4622, https://doi.org/10.1002/2015GL064040, 2015.

Garrett, T. J., Singh, D. K., and Pardyjak, E. R.: Settling and Rotation of Frozen Hydrometeors in Turbulent Air, Geophysical Research Letters, 52, e2025GL114780, https://doi.org/10.1029/2025GL114780, 2025.

Gong, J. and Wu, D. L.: Microphysical properties of frozen particles inferred from Global Precipitation Measurement (GPM) Microwave Imager (GMI) polarimetric measurements, Atmos. Chem. Phys., 17, 2741–2757, https://doi.org/10.5194/acp-17-2741-2017, 2017.

Greenler, R.: Rainbows, Halos, and Glories Cambridge U, Press, Cambridge, UK, 8–10, 1980.

Griesche, H. J., Seifert, P., Ansmann, A., Baars, H., Barrientos Velasco, C., Bühl, J., Engelmann, R., Radenz, M., Zhenping, Y., and Macke, A.: Application of the shipborne remote sensing supersite OCEANET for profiling of Arctic aerosols and clouds during *Polarstern* cruise PS106, Atmospheric Measurement Techniques, 13, 5335–5358, https://doi.org/10.5194/amt-13-5335-2020, 2020.

https://doi.org/10.5194/egusphere-2026-3314
Preprint. Discussion started: 16 June 2026

Hajipour, M.: Identification of hydrometeor types in Doppler spectra from polarimetric cloud radar observations, Ph. D. thesis, University of Leipzig, Leipzig, Germany, 2025.

Hamel, A., Schnaiter, M., Saito, M., Wagner, R., and Järvinen, E.: Cloud Chamber Studies on the Linear Depolarisation Ratio of Small Cirrus Ice Crystals, Atmos. Chem. Phys., 26, 1277–1300, https://doi.org/10.5194/acp-26-1277-2026, 2026.

He, Y., Liu, F., Yin, Z., Zhang, Y., Zhan, Y., and Yi, F.: Horizontally oriented ice crystals observed by the synergy of zenith- and slant-pointed polarization lidar over Wuhan (30.5°N, 114.4°E), China, Journal of Quantitative Spectroscopy and Radiative Transfer, 268, 107626, https://doi.org/10.1016/j.jqsrt.2021.107626, 2021.

Heymsfield, A. J. and Iaquinta, J.: Cirrus crystal terminal velocities, Journal of the Atmospheric Sciences, 57, 916–938, https://doi.org/10.1175/1520-0469(2000)057%3C0916:CCTV%3E2.0.CO;2, 2000.

Heymsfield, A. J., Krämer, M., Luebke, A., Brown, P., Cziczo, D. J., Franklin, C., Lawson, P., Lohmann, U., McFarquhar, G., Ulanowski, Z., and Van Tricht, K.: Cirrus Clouds, Meteorological Monographs, 58, 2.1-2.26, https://doi.org/10.1175/AMSMONOGRAPHS-D-16-0010.1, 2017.

Hu, Y., Winker, D., Vaughan, M., Lin, B., Omar, A., Trepte, C., Flittner, D., Yang, P., Nasiri, S. L., Baum, B., Holz, R., Sun, W., Liu, Z., Wang, Z., Young, S., Stamnes, K., Huang, J., and Kuehn, R.: CALIPSO/CALIOP cloud phase discrimination algorithm, Journal of Atmospheric and Oceanic Technology, 26, 2293–2309, https://doi.org/10.1175/2009JTECHA1280.1, 2009.

Jimenez, C., Ansmann, A., Engelmann, R., Donovan, D., Malinka, A., Seifert, P., Wiesen, R., Radenz, M., Yin, Z., Bühl, J., Schmidt, J., Barja, B., and Wandinger, U.: The dual-field-of-view polarization lidar technique: a new concept in monitoring aerosol effects in liquid-water clouds – case studies, Atmos. Chem. Phys., 20, 15265–15284, https://doi.org/10.5194/acp-20-15265-2020, 2020a.

Jimenez, C., Ansmann, A., Engelmann, R., Donovan, D., Malinka, A., Schmidt, J., Seifert, P., and Wandinger, U.: The dual-field-of-view polarization lidar technique: a new concept in monitoring aerosol effects in liquid-water clouds – theoretical framework, Atmos. Chem. Phys., 20, 15247–15263, https://doi.org/10.5194/acp-20-15247-2020, 2020b.

Kaur, I., Eriksson, P., Barlakas, V., Pfreundschuh, S., and Fox, S.: Fast Radiative Transfer Approximating Ice Hydrometeor Orientation and Its Implication on IWP Retrievals, Remote Sensing, 14, 1594, https://doi.org/10.3390/RS14071594, 2022.

Kennedy, S.: Astral: Calculations for the position of the sun and moon (Version 3.2), GitHub [code], https://github.com/sffjunkie/astral, 2023.

Kikuchi, M., Okamoto, H., and Sato, K.: A Climatological View of Horizontal Ice Plates in Clouds: Findings From Nadir and Off-Nadir CALIPSO Observations, Journal of Geophysical Research: Atmospheres, 126, 1–20, https://doi.org/10.1029/2020JD033562, 2021.

Klotzsche, S. and Macke, A.: Influence of crystal tilt on solar irradiance of cirrus clouds, Applied Optics, 45, 1034–1040, https://doi.org/10.1364/AO.45.001034, 2006.

https://doi.org/10.5194/egusphere-2026-3314
Preprint. Discussion started: 16 June 2026

Kokhanenko, G. P., Balin, Y. S., Klemasheva, M. G., Nasonov, S. V., Novoselov, M. M., Penner, I. E., and Samoilova, S. V.: Scanning polarization lidar LOSA-M3: opportunity for research of crystalline particle orientation in the ice clouds, Atmos. Meas. Tech., 13, 1113–1127, https://doi.org/10.5194/amt-13-1113-2020, 2020.

Krämer, M., Rolf, C., Spelten, N., Afchine, A., Fahey, D., Jensen, E., Khaykin, S., Kuhn, T., Lawson, P., Lykov, A., Pan, L. L., Riese, M., Rollins, A., Stroh, F., Thornberry, T., Wolf, V., Woods, S., Spichtinger, P., Quaas, J., and Sourdeval, O.: A microphysics guide to cirrus – Part 2: Climatologies of clouds and humidity from observations, Atmos. Chem. Phys., 20, 12569–12608, https://doi.org/10.5194/acp-20-12569-2020, 2020.

Li, H.: Growth and Melting of Atmospheric Ice Particles: Insights from Radar Observations, Ph.D. thesis, University of Helsinki, Helsinki, Finland, 2021.

Li, H., Korolev, A., and Moisseev, D.: Supercooled liquid water and secondary ice production in Kelvin–Helmholtz instability as revealed by radar Doppler spectra observations, Atmos. Chem. Phys., 21, 13593–13608, https://doi.org/10.5194/acp-21-13593-2021, 2021.

List, R. and Schemenauer, R. S.: Free-Fall Behavior of Planar Snow Crystals, Conical Graupel and Small Hail, J. Atmos. Sci., 28, 110–115, https://doi.org/10.1175/1520-0469(1971)028%3C0110:FFBOPS%3E2.0.CO;2, 1971.

MacPherson, J. I. and Baumgardner, D.: Airflow about King Air Wingtip-Mounted Cloud Particle Measurement Probes, J. Atmos. Oceanic Technol., 5, 259–273, https://doi.org/10.1175/1520-0426(1988)005%3C0259:AAKAWM%3E2.0.CO;2, 1988.

Mann, H. B. and Whitney, D. R.: On a Test of Whether one of Two Random Variables is Stochastically Larger than the Other, The Annals of Mathematical Statistics, 18, 50–60, https://doi.org/10.1214/AOMS/1177730491, 1947.

Marshak, A., Várnai, T., and Kostinski, A.: Terrestrial glint seen from deep space: Oriented ice crystals detected from the Lagrangian point, Geophysical Research Letters, 44, 5197–5202, https://doi.org/10.1002/2017GL073248, 2017.

Massey Jr., F. J.: The Kolmogorov-Smirnov test for goodness of fit, Journal of the American statistical Association, 46, 68–78, https://doi.org/10.1080/01621459.1951.10500769, 1951.

Masuda, K. and Ishimoto, H.: Influence of particle orientation on retrieving cirrus cloud properties by use of total and polarized reflectances from satellite measurements, Journal of Quantitative Spectroscopy and Radiative Transfer, 85, 183–193, https://doi.org/10.1016/S0022-4073(03)00224-3, 2004.

Mitchell, D. L.: Use of Mass- and Area-Dimensional Power Laws for Determining Precipitation Particle Terminal Velocities, J. Atmos. Sci., 53, 1710–1723, https://doi.org/10.1175/1520-0469(1996)053%3C1710:UOMAAD%3E2.0.CO;2, 1996.

Noel, V. and Chepfer, H.: Study of Ice Crystal Orientation in Cirrus Clouds Based on Satellite Polarized Radiance Measurements, J. Atmos. Sci., 61, 2073–2081, https://doi.org/10.1175/1520-0469(2004)061%3C2073:SOICOI%3E2.0.CO;2, 2004.

Noel, V. and Chepfer, H.: A global view of horizontally oriented crystals in ice clouds from Cloud-Aerosol Lidar and Infrared Pathfinder Satellite Observation (CALIPSO), Journal of Geophysical Research: Atmospheres, 115, 0–23, https://doi.org/10.1029/2009JD012365, 2010.

https://doi.org/10.5194/egusphere-2026-3314
Preprint. Discussion started: 16 June 2026

Pan, Z., Mao, F., Gong, W., Wang, W., and Yang, J.: Observation of clouds macrophysical characteristics in China by CALIPSO, J. Appl. Remote Sens, 10, 036028, https://doi.org/10.1117/1.JRS.10.036028, 2016.

Platt, C. M. R.: Lidar Backscatter from Horizontal Ice Crystal Plates, J. Appl. Meteor., 17, 482–488, https://doi.org/10.1175/1520-0450(1978)017%3C0482:LBFHIC%3E2.0.CO;2, 1978.

Pruppacher, H. R. and Klett, J. D.: Microphysics of Clouds and Precipitation, Springer Netherlands, Dordrecht, https://doi.org/10.1007/978-0-306-48100-0, 2010.

Radenz, M., Bühl, J., Seifert, P., Baars, H., Engelmann, R., Barja González, B., Mamouri, R.-E., Zamorano, F., and Ansmann, A.: Hemispheric contrasts in ice formation in stratiform mixed-phase clouds: disentangling the role of aerosol and dynamics with ground-based remote sensing, Atmospheric Chemistry and Physics, 21, 17969–17994, 2021.

Romano, J., Kromrey, J. D., Coraggio, J., and Skowronek, J.: Appropriate statistics for ordinal level data: Should we really be using t-test and Cohen's d for evaluating group differences on the NSSE and other surveys, in: Proceedings of the Annual Meeting of the Florida Association of Institutional Research, 2006.

Ross, A., Holz, R. E., and Ackerman, S. A.: Correlations of oriented ice and precipitation in marine midlatitude low clouds using collocated CloudSat, CALIOP, and MODIS observations, Journal of Geophysical Research: Atmospheres, 122, 8056–8070, https://doi.org/10.1002/2016JD026407, 2017.

Saito, M. and Yang, P.: Oriented ice crystals: a single-scattering property database for applications to lidar and optical phenomenon simulations, Journal of the Atmospheric Sciences, 76, 2635–2652, https://doi.org/10.1175/JAS-D-19-0031.1, 2019.

Sassen, K.: The Polarization Lidar Technique for Cloud Research: A Review and Current Assessment, Bull. Amer. Meteor. Soc., 72, 1848–1866, https://doi.org/10.1175/1520-0477(1991)072%3C1848:TPLTFC%3E2.0.CO;2, 1991.

Seifert, P.: Dust-related ice formation in the troposphere: A statistical analysis based on 11 years of lidar observations of aerosols and clouds over Leipzig, Ph.D. thesis, University of Leipzig, Leipzig, Germany, 2011.

Shao, N., Wang, Q., Bu, Z., Yin, Z., Dai, Y., Chen, Y., and Wang, X.: China Aerosol Raman Lidar Network (CARLNET)—Part I: Water Vapor Raman Channel Calibration and Quality Control, Remote Sensing, 17, 414, https://doi.org/10.3390/rs17030414, 2025.

Shimizu, A., Nishizawa, T., Jin, Y., Kim, S.-W., Wang, Z., Batdorj, D., and Sugimoto, N.: Evolution of a lidar network for tropospheric aerosol detection in East Asia, Opt. Eng, 56, 031219, https://doi.org/10.1117/1.OE.56.3.031219, 2016.

Shupe, M. D., Brooks, I. M., and Canut, G.: Evaluation of turbulent dissipation rate retrievals from Doppler Cloud Radar, Atmos. Meas. Tech., 5, 1375–1385, https://doi.org/10.5194/amt-5-1375-2012, 2012.

Silber, I., Fridlind, A. M., Verlinde, J., Ackerman, A. S., Cesana, G. V., and Knopf, D. A.: The prevalence of precipitation from polar supercooled clouds, Atmos. Chem. Phys., 21, 3949–3971, https://doi.org/10.5194/acp-21-3949-2021, 2021.

Stephens, G. L.: Remote sensing of the lower atmosphere: an introduction, Oxford University Press, New York, 523 pp., 1994.

https://doi.org/10.5194/egusphere-2026-3314
Preprint. Discussion started: 16 June 2026

Stout, J. R., Westbrook, C. D., Stein, T. H. M., and McCorquodale, M. W.: Stable and unstable fall motions of plate-like ice crystal analogues, Atmospheric Chemistry and Physics, 24, 11133–11155, https://doi.org/10.5194/ACP-24-11133-2024, 2024.

Takano, Y. and Liou, K.-N.: Solar radiative transfer in cirrus clouds. Part I: Single-scattering and optical properties of hexagonal ice crystals, Journal of Atmospheric Sciences, 46, 3–19, https://doi.org/10.1175/1520-0469(1989)046%3C0003:SRTICC%3E2.0.CO;2, 1989.

Tape, W. (Ed.): Atmospheric Halos, American Geophysical Union, Washington, D. C., https://doi.org/10.1029/AR064, 1994.

Varnai, T., Marshak, A., and Kostinski, A. B.: Deep Space Observations of Cloud Glints: Spectral and Seasonal Dependence, IEEE Geosci. Remote Sensing Lett., 19, 1–5, https://doi.org/10.1109/LGRS.2020.3040144, 2020.

Várnai, T., Marshak, A., Kostinski, A. B., Yang, Y., and Zhou, Y.: Impacts of Sun Glint Off Ice Clouds on DSCOVR EPIC Cloud Products, IEEE Trans. Geosci. Remote Sensing, 62, 1–11, https://doi.org/10.1109/TGRS.2024.3400253, 2024.

Virtanen, P., Gommers, R., Oliphant, T. E., Haberland, M., Reddy, T., Cournapeau, D., Burovski, E., Peterson, P., Weckesser, W., Bright, J., van der Walt, S. J., Brett, M., Wilson, J., Millman, K. J., Mayorov, N., Nelson, A. R. J., Jones, E., Kern, R., Larson, E., Carey, C. J., Polat, İ., Feng, Y., Moore, E. W., VanderPlas, J., Laxalde, D., Perktold, J., Cimrman, R., Henriksen, I., Quintero, E. A., Harris, C. R., Archibald, A. M., Ribeiro, A. H., Pedregosa, F., van Mulbregt, P., and SciPy 1.0 Contributors: SciPy 1.0: fundamental algorithms for scientific computing in Python, Nat. Methods, 17, 261–272, https://doi.org/10.1038/s41592-019-0686-2, 2020.

Wang, N., Zhang, K., Shen, X., Wang, Y., Li, J., Li, C., Mao, J., Malinka, A., Zhao, C., Russell, L. M., Guo, J., Gross, S., Liu, C., Yang, J., Chen, F., Sijie Chen1, L. W., Ke, J., Xiao, D., Zhou, Y., Fang, J., and Liu, D.: Dual-field-of-view high-spectral-resolution lidar: Simultaneous profiling of aerosol and water cloud to study aerosol-cloud interaction, Proceedings of the National Academy of Sciences of the United States of America, 119, e2110756119, https://doi.org/10.1073/PNAS.2110756119/SUPPL_FILE/PNAS.2110756119.SAPP.PDF, 2022.

Welton, E. J., Campbell, J. R., Spinhirne, J. D., and Scott Iii, V. S.: Global monitoring of clouds and aerosols using a network of micropulse lidar systems, Second International Asia-Pacific Symposium on Remote Sensing of the Atmosphere, Environment, and Space, 151, https://doi.org/10.1117/12.417040, 2001.

Westbrook, C. D.: The fall speeds of sub-100 µm ice crystals, Quart J Royal Meteoro Soc, 134, 1243–1251, https://doi.org/10.1002/qj.290, 2008.

Westbrook, C. D., Illingworth, A. J., O'Connor, E. J., and Hogan, R. J.: Doppler lidar measurements of oriented planar ice crystals falling from supercooled and glaciated layer clouds, Quarterly Journal of the Royal Meteorological Society, 136, 260–276, https://doi.org/10.1002/QJ.528, 2010.

Whitehead, L. E., McDonald, A. J., and Guyot, A.: Supercooled liquid water cloud classification using lidar backscatter peak properties, Atmos. Meas. Tech., 17, 5765–5784, https://doi.org/10.5194/amt-17-5765-2024, 2024.

https://doi.org/10.5194/egusphere-2026-3314
Preprint. Discussion started: 16 June 2026

Wu, Z., Seifert, P., He, Y., Baars, H., Li, H., Jimenez, C., Li, C., and Ansmann, A.: Assessment of horizontally oriented ice crystals with a combination of multiangle polarization lidar and cloud Doppler radar, Atmospheric Measurement Techniques, 18, 3611–3634, https://doi.org/10.5194/amt-18-3611-2025, 2025.

Wu, Z., Li, C., He, Y., Baars, H., and Seifert, P.: Horizontally Oriented Ice Crystals Observed with the Combination of Zenith and 15-degree off-Zenith pointing Polarization Lidar over Beijing (116.3°E 40.0°N), China, EPJ Web Conf., 362, 02021, https://doi.org/10.1051/epjconf/202636202021, 2026.

Yang, F., Cruikshank, O., He, W., Kostinski, A., and Shaw, R. A.: Nonthermal ice nucleation observed at distorted contact lines of supercooled water drops, Phys. Rev. E, 97, 023103, https://doi.org/10.1103/PhysRevE.97.023103, 2018.

Yang, P., Wei, H., Huang, H.-L., Baum, B. A., Hu, Y. X., Kattawar, G. W., Mishchenko, M. I., and Fu, Q.: Scattering and absorption property database for nonspherical ice particles in the near- through far-infrared spectral region, Appl. Opt., 44, 5512, https://doi.org/10.1364/AO.44.005512, 2005.

Zeng, X., Skofronick-Jackson, G., Tian, L., Emory, A. E., Olson, W. S., and Kroodsma, R. A.: Analysis of the Global Microwave Polarization Data of Clouds, Journal of Climate, 32, 3–13, https://doi.org/10.1175/JCLI-D-18-0293.1, 2019.

Zeng, X., Heymsfield, A. J., Ulanowski, Z., Neely Iii, R. R., Li, X., Gong, J., and Wu, D. L.: The Radiative Effect on Cloud Microphysics from the Arctic to the Tropics, Bulletin of the American Meteorological Society, https://doi.org/10.1175/BAMS-D-21-0039.1, 2022.

Zhang, H., Ramelli, F., Fuchs, C., Omanovic, N., Miller, A. J., Spirig, R., Wu, Z., Chu, Y., Li, X., Lohmann, U., and Henneberger, J.: Inferring the controlling factors of ice aggregation from targeted cloud seeding experiments, Atmospheric Chemistry and Physics, 26, 1459–1481, https://doi.org/10.5194/acp-26-1459-2026, 2026a.

Zhang, Y., Li, H., Wu, Z., Yao, F., Shu, Z., Yin, M., Ge, Y., Huang, Y., Wang, Z., and Zhang, W.: Classification of Cloud Phases in Cold-Air Outbreak Events Based on Polarization Lidar and Cloud Radar Observations, IEEE Trans. Geosci. Remote Sensing, 64, 1–14, https://doi.org/10.1109/TGRS.2026.3663561, 2026b.

Zhao, C., Wang, Y., Wang, Q., Li, Z., Wang, Z., and Liu, D.: A new cloud and aerosol layer detection method based on micropulse lidar measurements, Journal of Geophysical Research, 119, 6788–6802, https://doi.org/10.1002/2014JD021760, 2014.

Zhou, C., Yang, P., Dessler, A. E., and Liang, F.: Statistical properties of horizontally oriented plates in optically thick clouds from satellite observations, IEEE Geoscience and Remote Sensing Letters, 10, 986–990, https://doi.org/10.1109/LGRS.2012.2227451, 2012a.

Zhou, C., Yang, P., Dessler, A. E., Hu, Y., and Baum, B. A.: Study of horizontally oriented ice crystals with CALIPSO observations and comparison with Monte Carlo radiative transfer simulations, Journal of Applied Meteorology and Climatology, 51, 1426–1439, https://doi.org/10.1175/JAMC-D-11-0265.1, 2012b.